Quaternary Geochronology 82 (2024) 101551

Contents lists available at ScienceDirect

Quaternary Geochronology

journal homepage: www.elsevier.com/locate/quageo

Research paper

Luminescence dating of glacially sourced deposits from northern Switzerland: Comparing multigrain aliquots and single grains of quartz and feldspar

Daniela Mueller [a,*], Lukas Gegg [b], Alexander Fülling [a], Marius W. Buechi [b], Gaudenz Deplazes [c], Frank Preusser [a]

[a] Institute of Earth and Environmental Sciences, University of Freiburg, Albertstr. 23b, 79104 Freiburg, Germany
[b] Institute of Geological Sciences & Oeschger Centre for Climate Change Research, University of Bern, Baltzerstrasse 1+3, 3012 Bern, Switzerland
[c] NAGRA - Nationale Genossenschaft für die Lagerung Radioaktiver Abfälle, Hardstrasse 73, 5430 Wettingen, Switzerland

ARTICLE INFO

Keywords:
Pleistocene deposits
Quartz
Feldspar
Multi grain dating
Single grain dating

ABSTRACT

A complex picture of the Pleistocene glaciation history of northern Switzerland has been identified over the last three decades. To gain further insights into the long-term landscape evolution, numerical dating is required. In the absence of alternative dating techniques, luminescence dating is the key method for establishing chronological constraints of past glaciations. However, this is presented with complex challenges, especially in regard to the resetting of the luminescence signal prior to deposition, the components contributing to the signal as well as the signal intensity and stability. In this study, the luminescence properties of glacially sourced deposits from northern Switzerland are assessed using single aliquot (SA) and single grain (SG) measurements of feldspar (F) and quartz (Q). While no obvious connection between bleaching and distal or proximal deposition in relation to the proposed ice margin is observed, most samples seem to reveal a partially bleached signature in F SG D_e measurements. This appears to be masked in the respective F SA measurements even though only few grains emit luminescence signals. In addition, comparisons between fading corrected infrared stimulated luminescence (IR) and post-infrared infrared stimulated luminescence (pIR) D_e values appear to be unreliable indicators of bleaching, even though these signals bleach at different rates. Hence, it is recommended to conduct both IR and pIR investigations in combination with Q measurements on a SG level. The dating potential of the investigated deposits remains rather limited, yet, in the sedimentologic context the presented results reveal that several glacial advances occurred prior to the Last Interglacial in the study area.

1. Introduction

Over the last three decades, a much more complex picture of the timing and extent of Pleistocene glaciations of the northern foreland of the Central Alps than previously assumed has been identified (cf. Preusser et al., 2011). Although some glacial advances have apparently reached into the lowlands, a consensus regarding their exact number and timing remains elusive. While the ice advances of the last glacial maximum (LGM) have been relatively well constrained through field evidence and numerical dating (Gaar et al., 2019; Gribenski et al., 2021; Kamleitner et al., 2022), this level of understanding does not extend to the older glaciations of the Middle and Early Pleistocene. Research into this topic has been stimulated by considerations related to the siting of nuclear waste disposal sites, in Switzerland and beyond. As the long-term safety of such sites might be challenged by the formation of overdeepened structures through subglacial erosion (e.g., Preusser et al., 2010; Anselmetti et al., 2022; Gegg and Preusser, 2023), this issue has moved into the focus of the responsible agencies (Breuer et al., 2023; Cohen et al., 2023; Müller et al., 2023). A challenging but central issue in this context is establishing an independent and reliable chronological framework.

In the absence of alternative dating techniques for such deposits, luminescence dating is the key method for establishing chronological constraints on past glaciations (cf. Thrasher et al., 2009), particularly for northern Switzerland (e.g., Preusser, 1999a; Kock et al., 2009; Dehnert et al., 2012; Lowick et al., 2015; Buechi et al., 2018). However, the

* Corresponding author.
E-mail address: daniela.mueller@liverpool.ac.uk (D. Mueller).

https://doi.org/10.1016/j.quageo.2024.101551
Received 14 November 2023; Received in revised form 11 April 2024; Accepted 27 May 2024
Available online 2 June 2024

dating of glacially sourced deposits using this approach is presented with complex challenges (Duller, 1994, 2006; Spencer and Owen, 2004). Such environments often exhibit sediment sources and sinks in close proximity, reducing the transport distance. Furthermore, transportation may occur in ice or turbid water, which limits the exposure of grains to sufficient sunlight required to reset or bleach any pre-existing luminescence signals. Consequently, this effect can lead to age overestimation and requires careful consideration in dating such deposits. Quartz (Q) is most often favoured as a dosimeter in optically stimulated luminescence (OSL) dating due to its more readily bleachable nature compared to feldspar (F) (Godfrey-Smith et al., 1988; Murray et al., 2012). Another advantage of Q is that the luminescence signal is considered stable over long periods of time (Murray and Wintle, 1999). However, for Q from the wider region, certain samples have exhibited unstable components (e.g., Trauerstein et al., 2017), while others have not (e.g., Gaar et al., 2013). Furthermore, laboratory dose response curves (DRC) for Q have often shown a double-saturating exponential behaviour that accounts for high dose responses beyond single exponential behaviour (Lowick et al., 2010; Dehnert et al., 2012). This phenomenon has been observed in samples, where luminescence ages either agree (e.g., Murray et al., 2008; Pawley et al., 2010) or disagree (e.g., Lai, 2010; Timar et al., 2010; Timar-Gabor et al., 2011) with independent age control. However, the underlying cause of this behaviour remains unidentified (Wintle, 2008). In northern Switzerland, Q luminescence ages have been obtained up to approximately 200 ka (Anselmetti et al., 2010; Dehnert et al., 2012; Lowick et al., 2015; Buechi et al., 2017). Nevertheless, this time range is insufficient for establishing a chronology of the Mid-Pleistocene glaciation history (Graf, 2009a; Preusser et al., 2011).

In contrast to Q, F requires more time to reset its signal prior to deposition, but is capable of dating much older deposits than Q, as it saturates at higher doses (Duller, 1997). However, the infrared stimulated luminescence (IRSL or IR) signal of F measured at 50 °C often suffers from anomalous fading, leading to age underestimation (Wintle, 1973; Spooner, 1994). Various approaches, which rely on observations of signal loss in laboratory experiments conducted over hours-to-days to deduce signal loss occurring over geological timescales, have been proposed to determine and account for signal loss over time, (Huntley and Lamothe, 2001; Auclair et al., 2003; Lamothe et al., 2003; Huntley, 2006; Kars et al., 2008). In storage tests, fading rates between 1% and 3% per decade (Dehnert et al., 2012; Lowick et al., 2012, 2015; Gaar and Preusser, 2012; Buechi et al., 2017) were observed for most samples from northern Switzerland. However, in some cases, uncorrected IR D_e values were beyond the linear part of the DRC, making them unsuitable for most fading correction approaches. Corrected IR (IR_{corr}) D_e values were close to saturation and consequently rejected for age determination, or uncorrected F ages were in better agreement with Q ages and, therefore, favoured (Dehnert et al., 2012; Lowick et al., 2012, 2015; Gaar and Preusser, 2012; Buechi et al., 2017). Gaar et al. (2013) and Mueller et al. (2020) were the only ones who reported that correcting for fading was appropriate and necessary for samples younger than 100 ka or up to 200 ka, respectively.

To address the dating of older samples, Lowick et al. (2012) conducted experiments with alternative measurement protocols targeting signals more stable than the IR signal, specifically the post-infrared infrared stimulated luminescence signals (pIRIR or pIR). The pIR signals are measured at higher temperatures following an initial readout of the IR signal at 50 °C. While fading is expected to decrease or become negligible for the more stable pIR signals, these signals require longer sunlight exposure to bleach during transportation (Thomsen et al., 2008; Buylaert et al., 2011; Thiel et al., 2011a, 2011b). Indeed, Lowick et al. (2012) observed age overestimations compared to independent age control when using pIR_{225} and pIR_{290} signals from multi-grain measurements on large aliquots, leading to the conclusion that these approaches are not advantageous for dating the investigated water-lain sediments from northern Switzerland. To address this problem, the measurement of single grains (SG) or small, single aliquots (SA) has been recommended to monitor equivalent dose (D_e) distributions, and to isolate well-bleached portions of these distributions (e.g., Olley et al., 2004; Duller, 2006; Trauerstein et al., 2017).

In this study, the luminescence properties of glacially sourced (glaciolacustrine, glaciodeltaic, glaciofluvial, and periglacial) deposits from the Lower Aare Valley, the adjacent Rinikerfeld and the Strassberg Trough, which are all located in the northern foreland of the Swiss Alps, are assessed. Outcrop sampling and scientific drilling was conducted at stratigraphic key sites within the former glacier forefield as part of a larger project aiming to gain further insights into the long-term glacial and fluvial landscape evolution of northern Switzerland.

As the SA approach is the most used in such environments (e.g. Klasen et al., 2016; Ali et al., 2022; Schwenk et al., 2022), it has been investigated first for coarse-grained Q and F extracts. Performance tests, signal intensity and composition (Q only), as well as the fading properties and bleachability of IR and pIR signals are presented and discussed. Results are then compared with those of SG measurements to address partial bleaching and to explore the dating potential of the investigated deposits and similar ones found elsewhere. Implications of the derived ages for landscape evolution will be discussed further in an additional publication. For this, and to provide information regarding the differing depositional conditions, detailed site descriptions are given first.

2. Study sites and samples

The Lower Aare Valley and Rinikerfeld study areas are located in the easternmost foothills of the Jura Mountains in central northern Switzerland, some 50 km northwest of the Alpine front (Fig. 1A and B). The pre-Quaternary bedrock consists of Jurassic marls and limestones that are locally overlain by Palaeogenic to Neogenic sedimentary rock of the Molasse Basin (Berger et al., 2005; Jordan et al., 2008). River valleys incised into the Jura Mountains (Ziegler and Fraefel, 2009) were repeatedly reached and overridden by glaciers advancing from the Alps during the Pleistocene (Preusser et al., 2011). These ice advances widened and locally overdeepened the valleys, leaving a diverse suite of glacially sourced and periglacial deposits behind (Graf, 2009a, 2009b).

The Lower Glatt Valley study area is located about 20 km east of the Lower Aare Valley, to the east of the Jura Mountains (Fig. 1A and C). This typical Swiss Plateau landscape is characterised by a low relief and gentle hills consisting mainly of Neogene Molasse bedrock. The repeated, extensive Alpine glacier advances during the Pleistocene shaped a complex network of buried troughs in the region (Wyssling, 2008; Graf, 2009a). A northwest trending segment of this network within the Lower Glatt Valley is the Strassberg Trough (Buechi et al., 2018; Haldimann et al., 2017).

Samples for the present study were obtained from sedimentary infills of the Lower Aare Valley, Rinikerfeld and the Strassberg Trough (Fig. 2). From the first two areas, drill cores (i.e. GBR, HST, UST) were collected during an extensive campaign (Gegg et al., 2019a, 2019b; Amschwand et al., 2020). At Rinikerfeld, a further drill core (RIN) was obtained to investigate the Habsburg-Rinikerfeld Palaeochannel (Gegg et al., 2018). This was complementary to samples collected from two hillslope outcrops (HABS, RINI) in the Lower Aare Valley (see SI 1).

2.1. Lower Aare Valley

The present-day Lower Aare Valley (Fig. 1B) accommodates the overdeepened Gebenstorf-Stilli Trough which is infilled largely by glaciolacustrine deposits overlying thin glaciogenic diamict and gravels (Gegg et al., 2021). Both have tentatively been attributed to the penultimate glaciation during Marine Isotope Stage (MIS) 6 by Graf (2009a). In the southern part of the trough, the infill consists of horizontally bedded to massive silty sand, indicating a deltaic to lacustrine environment. Occasional diamictic or gravelly interbeds contain

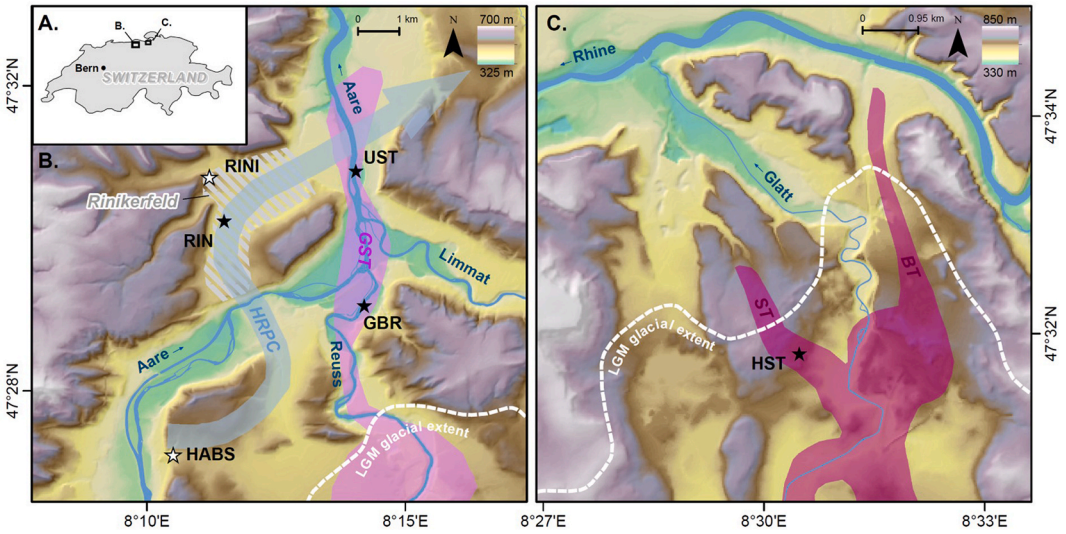

Fig. 1. A. Overview of the two study areas within northern Switzerland. Drilling locations (black stars) and outcrops (white stars) are shown. **B**. shows the Lower Aare Valley with the extent of the Gebenstorf-Stilli Trough (GST) and the direction of the Habsburg-Rinikerfeld Palaeochannel (HRPC) is indicated. The extent of the two bedrock overdeepenings within the Lower Glatt Valley, Strassberg Trough (ST) and Bülach Trough (BT), are shown in **C**.

ice-rafted debris and suggest an ice-proximal position (Gegg et al., 2019b). The material of sample GBR12 (91.6 m depth), crudely bedded light olive-grey silty sand, has likely been transported into the palaeolake by turbid melt water from subglacial and/or ice-marginal sources. In the northern part, coarse-grained gravels interfinger with the glaciolacustrine sand (Gegg et al., 2021). This is interpreted as meltwater gravels emplaced in a large delta, potentially delivered from a tributary valley to the north (Graf, 2009a). The sorting of this deltaic gravels varies considerably and the presence of poorly sorted intervals points towards rather short-scale glaciofluvial transport (Gegg et al., 2021). Sample UST3 (33.2 m depth) was taken from the top of a 1-m thick fining-upward sequence and consists of grey, moderately sorted fine gravelly and silty sand.

The glaciolacustrine trough infill is unconformably overlain by gravels which mark the lowest-lying fluvial deposits of the Lower Aare Valley. Samples GBR1 (11.2 m depth) and UST1 (13.2 m depth) have both been collected from the sandy tops of well-sorted fining-upward cycles. These two samples are expected to be the youngest deposits investigated in this study and are attributed to the Low Terrace depositional system that was supposedly active between MIS 6 and MIS 2 (Graf et al., 2006; Graf 2009a; Graf and Burkhalter, 2016).

2.2. Habsburg-Rinikerfeld Palaeochannel

The Habsburg-Rinikerfeld Palaeochannel (Fig. 1B) is part of an abandoned Mid-Pleistocene drainage network and hosts at least two, possibly three or more, units of glaciofluvial terrace deposits (Graf, 2009a). Two outcrops of glaciofluvial gravels contain well-sorted sand lenses that have been sampled for analysis; HABS1-3 consisting of beige, crudely cross-bedded very silty fine sand and RINI4-1 consisting of beige-grey bedded to cross-bedded silty sand. These sediments represent deposition from comparatively slow-flowing water offside the main channels of the braided river. This may indicate a rather distal setting, however, the ice margin position is not known. Those deposits have tentatively been placed into MIS 6 (Graf et al., 2006; Graf, 2009a). Both outcrops have later been overridden by glacial ice despite being located outside of the local LGM boundary. This is evident from glaciotectonic deformation in the HABS outcrop and from a till layer further up in the RINI outcrop (without a visible hiatus in between; cf. Graf, 2009a).

The Habsburg-Rinikerfeld Palaeochannel is most well pronounced in the Rinikerfeld. There, a small lake developed, which initially was in contact with an ice margin, but later was abandoned and fed by local runoff and occasional floods. This has chronologically been placed in the transition from MIS 7 to early MIS 6 (Mueller et al., 2020; Gegg et al., 2023; Table S2). RIN4, obtained from a depth of 9.0 m, consists of orange-beige clayey and silty sand that represents the last phase of deposition in the slowly silting-up lake basin. These palaeolake deposits are overlain by presumably periglacial colluvial diamict comprising reworked glacial and/or glaciofluvial material, as well as fragments of the local bedrock (Gegg et al., 2023). RIN2 (6.2 m depth) was taken from a massive ochre-beige slightly silty sand interbed of the colluvial sequence. Neither RIN2 nor RIN4 show evidence of glacial proximity.

2.3. Strassberg Trough

The Strassberg Trough is located in the modern Lower Glatt Valley (Fig. 1A and C) and is the western of two main bedrock overdeepenings which are nested into a 6–8 km wide valley (Buechi et al., 2018; Haldimann et al., 2017). The eastern lobe (Bülach Trough) is thought to have been eroded and infilled in multiple phases during MIS 6. It is overlain by a thick till-outwash complex emplaced during the last glacial cycle. The Strassberg Trough is also overlain by fluvial to glaciofluvial deposits and tills, which are suspected to be of MIS 6 age and older. This is as suggested by the local stratigraphic context and the luminescence dating of deposits in an equivalent stratigraphic position about 15 km upstream (Buechi et al., 2017, 2018). These deposits would predate those of the Bülach Trough, however, the infill of the Strassberg Trough has not yet been dated directly.

The entire overdeepened valley fill of the Strassberg Trough, including the overlying gravels and till, was recovered in about 267 m of drill cores (Amschwand et al., 2020). At the base, the infill consists of coarse-grained diamict and gravels that fine upward into stratified sand and silts. This succession is interpreted as a deglaciation sequence reflecting the transition from a highly dynamic subglacial and proximal proglacial lacustrine setting to an increasingly distal proglacial lake setting influenced by turbidity currents. Towards the top of this succession (ca. 141 m depth), one sample, HST15, was collected from a slightly silty, fine-medium sand unit.

The basal sequence is capped by an interbed of matrix-rich, glacial diamict representing a first glacial advance into the filling of the overdeepening. Above this, stratified glaciolacustrine to lacustrine silt and clay with occasional dropstones are found. Near the top contact, the fines are strongly deformed, consolidated and contain soft clasts. These are likely basin fill deposits that have been reworked during a further

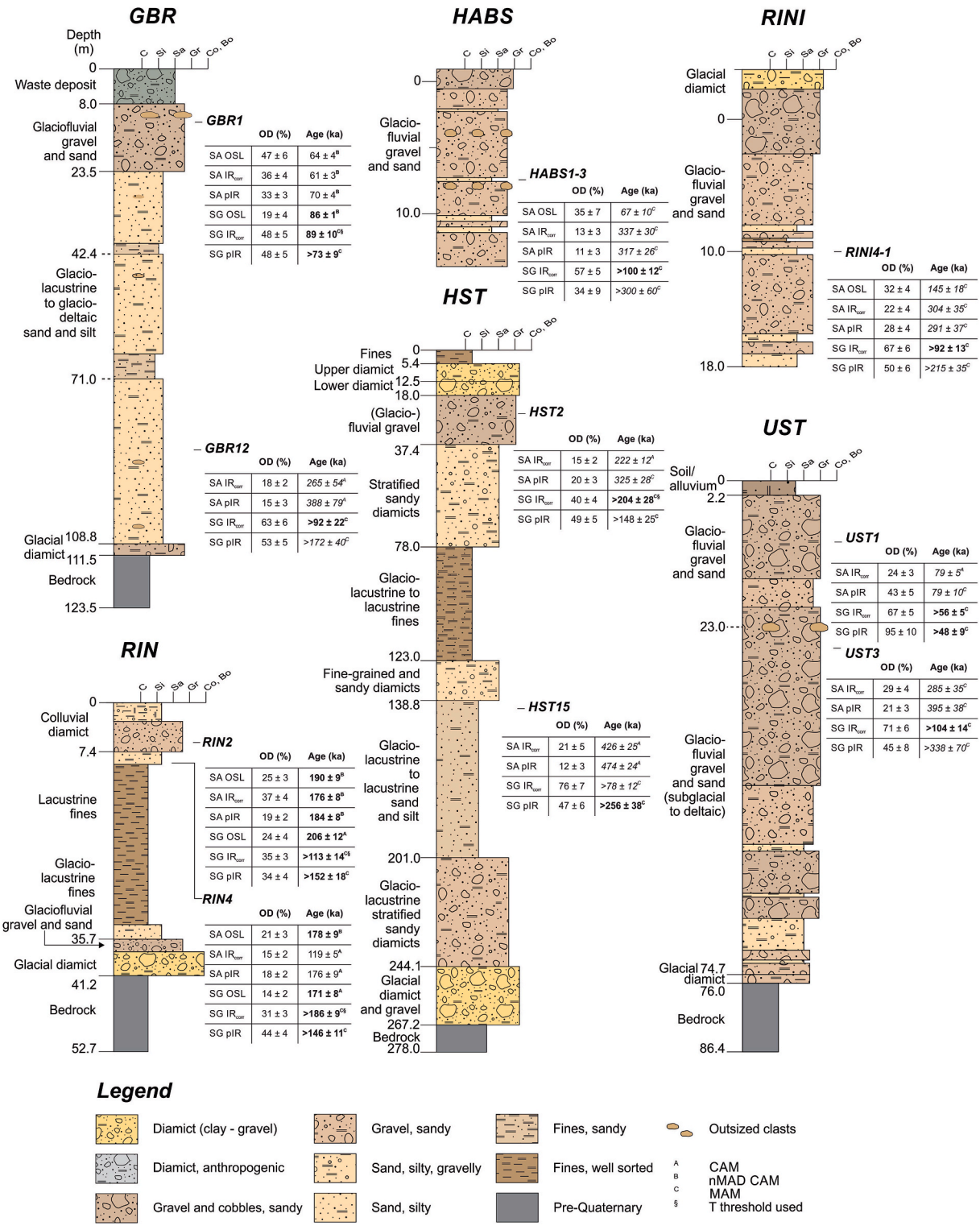

Fig. 2. Sedimentological logs of all drill cores and outcrops with luminescence sampling positions and ages derived using different luminescence signals. Ages in bold are those apparently most reliable. Ages with denoted ">" represent absolute minimum ages. For further discussion see section 6.2.

glacial advance and are topped with sandy diamict. Above an erosional contact, glaciofluvial gravels with occasional sand interbeds marks the transition into a non-overdeepened fluvial domain. Stratigraphically, these units can be correlated to a rather extensive gravel unit known from the Glatt Valley (equivalents to the Aarthal Gravel; Graf, 2009a; Buechi et al., 2018), and hence, sample HST2 was collected from an interbed of well-sorted, fine-medium sand. The gravels are capped by two gravel-rich glacial diamicts which are separated by a 1-m thick palaeosol. With the upper diamict unit likely being deposited during the last glaciation of the Lower Glatt Valley around the LGM (MIS2), and the lower weathered diamict representing an earlier extensive Middle Pleistocene glaciation (i.e., MIS 6 or older).

3. Material and methods

3.1. Sample preparation

For luminescence dating, samples were collected from outcrops (HABS, RINI; Fig. 2) using 20 cm aluminium tubes which were driven into the cleared outcrop surfaces. Only the inner, light-safe part of the tubes were used for D_e determination, discarding about 3 cm of both tube ends and the outer rind. For dose rate determination, sediment surrounding the sampling tubes was collected. Further samples were obtained from drill cores (GBR, HST, RIN, UST; Gegg et al., 2018; 2019a; 2019b; Amschwand et al., 2020). About 10 cm segments from previously split plastic liners (10 cm diameter) were collected, whereby the outer rind and the surface, potentially exposed during core cutting and splitting, were kept for dose rate determination and only the inner, light-safe core was used for D_e determination.

For D_e determination, all samples were wet-sieved and treated with HCl and H_2O_2 to remove carbonates and organic matter, respectively. Coarse grained (100–200 and 200–250 μm; Table S2) potassium-rich F and Q were separated using sodium polytungstate at densities of 2.58 g cm^{-3} and 2.70 g cm^{-3}. The Q grains were etched in 40% HF for 1 h to remove the outer rind, followed by a 20% HCl treatment for another hour to eliminate any fluoride precipitates. Grains were mounted either onto stainless-steel cups using silicon oil stamps with diameters of 1 mm for F and 2 mm and 4 mm for Q (ca. 10, 50 and 200 grains, respectively; Table S2) for SA measurements or onto aluminium discs with a 10*10 grid of holes (300 μm in diameter) for SG measurements.

3.2. Equipment

D_e values were obtained either with a Freiberg Instruments Lexsyg Research (Lexsyg ID 09 0020), a Freiberg Instruments Lexsyg Smart (Lexsyg ID 14 16 01 0010) or a Risø TL/OSL DA-20 (Reader ID 250; "Mönch"). Both Lexsyg readers use LEDs with peak emission at 458 nm for Q (50 mW/cm) and at 850 nm for F (130 mW/cm). Signals were detected by an ET 9235QB (Lexsyg Research) or a Hamamatsu H-7360 (Lexsyg Smart) photomultiplier tube after filtering through a 2.5 mm Hoya U-340 glass in combination with a 5 mm Delta-BP 365/50 EX-interference filter (Q) or a combination of a 3 mm BG39 Schott glass and a 3.5 mm HC 414/46-1 AHF Brightline interference filter (F). The latter was applied in combination with a cardboard barrier that was mounted into the filter wheel to prevent oversaturation of the photomultiplier tube (for details see Mueller et al., 2020). On the Risø reader, SA measurements were conducted with LED peak emissions at 470 nm for Q and at 850 nm for F while and an Nd:YVO_4 solid state diode-pumped laser emitting at 532 nm (Q) and an IR laser emitting at 830 nm (F; cut-off filter RG-780) were used for SG measurements. Stimulation was conducted using 90% power of the stimulation units. All signals were detected by an EMI 9235QB photomultiplier tube after passing through either a Hoya U-340 glass (Q SA: 7.5 mm; Q SG: 2.5 mm) or a combination of a 2 mm BG39 Schott glass and a D410/30 LOT/Oriel interference filter (SA and SG F).

Laboratory irradiation was given by $^{90}Sr/^{90}Y$ beta sources mounted into all three readers. All beta sources were calibrated using LexCal 2014 (calibration quartz of Freiberg Instruments) to ca. 0.12 Gy s^{-1} for both the Lexsyg Research and Lexsyg Smart and to ca. 0.10 Gy s^{-1} (SA) and ca. 0.09 Gy s^{-1} (SG) for the Risø reader. For further details on calibration please see SI 2.

It has previously been noted that the preheat behaviour of the Lexsyg Research reader used, at a heating rate of 5 °C s^{-1}, is specific and that the so-called 110 °C TL peak emerges at much lower temperatures than expected (ca. 87 °C; Mueller et al., 2020). However, comparison of both the Lexsyg Research and the Lexsyg Smart readers show TL counts peaking at equal temperatures during preheat. Also, as a means of internal laboratory quality control, D_e values were determined on both readers for a variety of samples and results are identical within

Table 1
Measurement protocols as used within this study. Temperatures used on the Lexsyg readers are shown in bold and those used on the Risø reader in italic.

Step	Q - SA[c]	Q - SG	F – SA[c]	F - SG	Signal
0	IRSL screening[a]				
1	Regenerative dose[b]	Regenerative dose[b]	Regenerative dose[b]	Regenerative dose[b]	
2	Preheat at **240**°C or*255*°C for 10 s	Preheat at *255*°C for 10 s	Preheat at **250**°C or *285*°C for 60 s	Preheat at *285*°C for 60 s	
3	OSL stimulation at **125**°C or *125*°C for 60 s	OSL stimulation at *125*°C for 2 s	IR stimulation at **50**°C or *50*°C for 300 s	IR stimulation at *50*°C for 1.6 s	OSL: L_n or L_x IR: L_n or L_x
4			IR stimulation at **225**°C or *240*°C for 200 s	IR stimulation at *240*°C for 1.6 s	pIR: L_n or L_x
5	Test dose[b]	Test dose[b]	Test dose*	Test dose[b]	
6	Preheat at **240**°C or *255*°C for 10 s	Preheat at *255*°C for 10 s	Preheat at **250**°C or *285*°C for 60 s	Preheat at *285*°C for 60 s	
7	IR stimulation at **50**°C or *50*°C for 40 s[+]	IR stimulation at *50*°C for 40 s[+]			
8			IR stimulation at **50**°C or *50*°C for 300 s	IR stimulation at *50*°C for 1.6 s	IR: T_n or T_x
9	OSL stimulation at **125**°C or *125*°C for 60 s	OSL stimulation at *125*°C for 2 s	IR stimulation at **225**°C or *240*°C for 200 s	IR stimulation at *240*°C for 1.6 s	OSL: T_n or T_x pIR: T_n or T_x

[+]only applied in the last regenerative dose step which had the same given dose as the first regenerative dose step following Duller (2003).
[a] Conducted for GBR1, HABS1-3 and UST1 prior to the L_n measurements.
[b] Omitted for the measurement of the natural signal.
[c] For measurements conducted on the Risø reader, temperatures were amended to match temperatures initially used on the Lexsyg devices – further information is provided in SI 4.

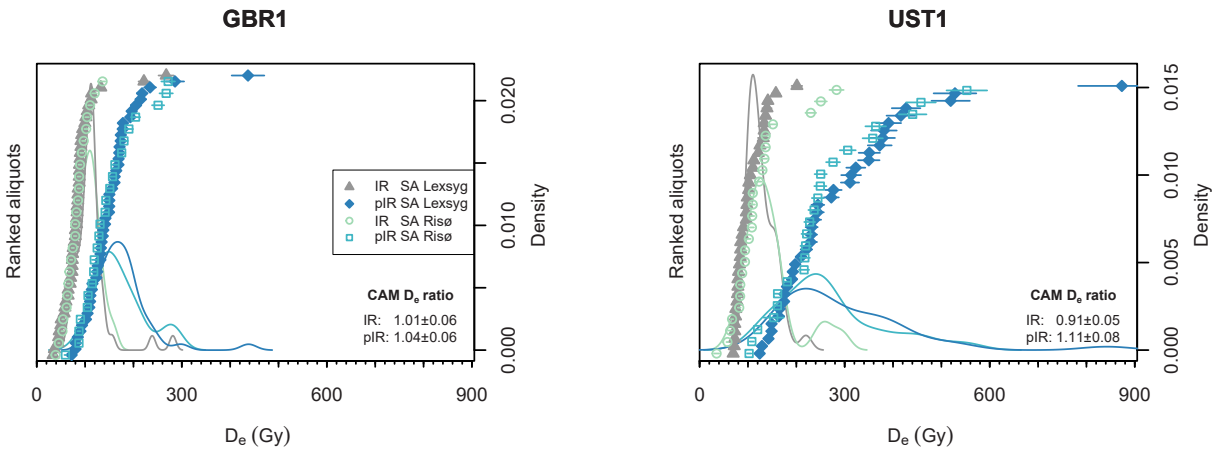

Fig. 3. Comparison of SA IR and pIR D_e values obtained on two different readers.

uncertainty of each other. This increased confidence in the consistency of the results derived using both machines. However, on the Risø reader used, the 110 °C TL peak is recorded at ca. 110 °C. To overcome this temperature discrepancy of over 20 °C, measurement protocols that were originally used on the Lexsyg readers were amended before they were used on the Risø reader. For further details see SI 4 and Figure S3.

To avoid bias introduced by using different reader types, the reproducibility of the measurement results was tested. For both Lexsyg readers, comparability of SA measurements was continuously monitored on a variety of samples as part of internal laboratory quality measures (data not presented). To assess the comparability between the Lexsyg and Risø readers, SA pIR measurements of two samples were duplicated on the Risø with an amended pIR protocol adjusted for differences in heating behaviour (see Table 1 and SI 4). For this, samples with the lowest expected D_e values, i.e. GBR1 and UST1, were chosen to prevent the impact of amplification of uncertainties by fitting in the high dose range. Obtained IR and pIR D_e distributions of both readers and samples present similar to almost identical shapes (Fig. 3). For GBR1, CAM D_e values are in good agreement (1 σ) with ratios of 1.01 ± 0.06 and 1.04 ± 0.06 for IR and pIR, respectively. In comparison, the D_e distribution of UST1 is characterised by a few outliers, especially in the higher D_e range and CAM D_e ratios of 0.91 ± 0.05 and 1.11 ± 0.08 were yielded for IR and pIR, respectively. After outlier exclusion (nMAD; Table S3) these ratios improve to 0.95 ± 0.07 for the IR signal. However, pIR results remain consistent at 2 σ with a ratio 1.18 ± 0.15 due to the wide spread of pIR values, which increases confidence in the reproducibility of results between readers.

3.3. D_e value determination

For D_e determination, the OSL signal of Q and IR as well as pIR signals of F were obtained (Table S3). F measurements were conducted using a $pIRIR_{225}$ protocol (amended from Thomsen et al., 2008) of which both signals were utilised and are hereafter called IR and pIR. Both Q and F measurements were conducted following the Single Aliquot Regenerative dose (SAR) protocol (Murray and Wintle, 2000) with administered test doses (T_n or T_x) of ca. 50 Gy and ca. 25 Gy, respectively. All protocols are presented in Table 1 and full SAR measurement were conducted on a number of aliquots or grains per sample (Table S4). In addition to SAR measurements, a shortened measurement (SM) protocol was used on a larger number of aliquots for some samples (Table S4) to accelerate measurements. For this, solely the natural and one regenerative dose were obtained. Full SAR measurements were utilised for some samples to construct a least-square (LS) normalised Standardised Growth Curve (SGC) following Li et al. (2015a, 2015b, 2016). The sensitivity-corrected natural signal (L_n/T_n) of both the SAR and SM protocols were projected onto the SGC after re-normalisation (cf. Mueller and Preusser, 2022). Protocol and SGC performances were tested on all samples and signals (Table S2).

For D_e determination, the initial signal was derived from the first 0.2 s and 0.1 s of the OSL and the first 15 s and 0.2 s of all IR and pIR signals, for SA and SG respectively. A late background subtraction using the last 40 s or 1.5 s (SA and SG OSL) and 50 s or 0.2 s (SA and SG IR) was applied, respectively. DRCs and SGCs were well fitted with a double-saturating exponential function ($f(x) = a(1 - \exp(-bx)) + c(1 - \exp(-dx)) + e$) and D_e values were derived using the numOSL package for R (Peng et al., 2018). Aliquots and grains that presented bright (T_n > 3*background level) and precise (T_n uncertainty <10%) test dose signals, low recycling ratio deviations (<20% SA, <10% SG; full SAR measurements only), a minor 0 Gy dose response (<5% of L_n/T_n; full SAR measurements only), IR depletion ratio deviations of <20% for SA and <10% for SG measurements (full SAR Q measurements only), well fitted DRCs or SGCs (full SAR measurements only; goodness-of-fit of figure-of merit (FOM <10; $FOM = \Sigma\left|y_i^o - y_i^f\right| / \Sigma y_i^f * 100$)) and fast component domination (>80%; SA Q only; see section 4.1) were accepted (see Table S4).

Mean D_e values were calculated using the Central and the three-parameter Minimum Age Models, CAM and MAM (SA $\sigma_b = 0.2$; SG $\sigma_b = 0.3$; assumed), respectively (Galbraith et al., 1999). In addition, the CAM was applied after outliers were removed using the normalised median absolute deviation (nMAD; Powell et al., 2002).

3.4. Dose rate determination

To determine the dose rates (Table 2), sample material was dried and radionuclide content was determined via high-resolution gamma-ray spectrometry at VKTA (Dresden, Germany). Radioactive disequilibrium was imperceptible (see $^{238}U/^{226}Ra$ ratio in Table 2; cf. Degering and Degering, 2020). A mean alpha efficiency factor of 0.05 ± 0.01 (Preusser, 1999a, 1999b; Preusser et al., 2001) and an internal potassium content of 12.5% ± 0.5% (Huntley and Baril, 1997) were assumed for all F fractions. The cosmic contribution was determined for present-day depths following Prescott and Hutton (1994). Water content relative to the dry weight of the sample were determined in the laboratory and representative long-term water content estimates were used for total dose rate (DR_{total}) determination. Those are estimated to be between 12% ± 4% and 20% ± 5% for both outcrops and core samples. DR_{total} range between 0.85 ± 0.05 Gy ka^{-1} and 1.96 ± 0.19 Gy ka^{-1} for Q and to 1.67 ± 0.08 Gy ka^{-1} and 2.54 ± 0.15 Gy ka^{-1} for F. DR_{total} and age calculations were conducted with ADELE 2017 software (www.addideas.com; Degering and Degering, 2020) accounting for machine uncertainties of 2%.

Table 2
Dosimetric data and total dose rates as used for age determination (all values are given with 1σ uncertainties).

Sample code	Sample depth (m)	WC field[A] (%)	WC used[A] (%)	Radionuclide concentrations			$^{238}U/^{226}Ra$	DR_{cosmic} (Gy ka^{-1})	DR_{total} Q (Gy ka^{-1})	DR_{total} F[B] (Gy ka^{-1})
				^{238}U (ppm)	^{232}Th (ppm)	^{40}K (%)				
GBR1	11.2	20	20 ± 5	1.21 ± 0.09	4.17 ± 0.30	0.99 ± 0.08	0.99 ± 0.17	0.07 ± 0.01	1.29 ± 0.12	2.12 ± 0.14
GBR12	91.6	12	20 ± 5	1.51 ± 0.10	4.19 ± 0.30	1.08 ± 0.09	0.88 ± 0.15	0.01 ± 0.01	–	2.18 ± 0.45
HABS1-3	8.0	18	12 ± 4	2.10 ± 0.13	5.58 ± 0.37	1.26 ± 0.13	0.86 ± 0.12	0.09 ± 0.01	1.96 ± 0.19	2.54 ± 0.15
HST2	27.6	6	15 ± 5	1.29 ± 0.09	3.38 ± 0.22	0.57 ± 0.06	0.92 ± 0.16	0.02 ± 0.01	–	1.76 ± 0.13
HST15	140.6	16	15 ± 5	1.45 ± 0.09	2.91 ± 0.20	0.78 ± 0.05	1.07 ± 0.14	0.01 ± 0.01	–	1.92 ± 0.09
RIN2	6.1	17	20 ± 5	0.69 ± 0.15	3.31 ± 0.22	0.53 ± 0.04	0.83 ± 0.19	0.11 ± 0.01	0.85 ± 0.05	1.67 ± 0.08
RIN4	9.0	18	20 ± 5	1.44 ± 0.26	4.90 ± 0.30	0.77 ± 0.05	1.10 ± 0.20	0.08 ± 0.01	1.19 ± 0.07	1.86 ± 0.07
RINI4-1	10.0	7	12 ± 4	1.19 ± 0.07	4.15 ± 0.25	1.09 ± 0.11	1.03 ± 0.14	0.08 ± 0.01	1.48 ± 0.20	2.31 ± 0.17
UST1	13.2	26	20 ± 5	1.35 ± 0.10	3.33 ± 0.25	0.96 ± 0.08	1.02 ± 0.19	0.06 ± 0.01	1.29 ± 0.06	2.06 ± 0.13
UST3	33.2	13	15 ± 5	1.28 ± 0.10	3.03 ± 0.25	0.62 ± 0.05	1.27 ± 0.27	0.02 ± 0.01	–	1.77 ± 0.12

[A]Water content as measured from the sample (field) and as used for D_e determination.
[B]Alpha efficiency of 0.05 ± 0.01 and internal potassium content of 12.5% ± 0.5% were assumed.

4. Luminescence signal properties

4.1. Signal properties of SA quartz

Initial SA testing of the sample's Q fractions revealed three different sample types. SA type 1 was found for RIN2, RIN4 and RINI4-1, which is characterised by a comparatively bright signal (example in Fig. 4A) that is fast component dominated (>80%; deconvolution following Bluszcz and Adamiec, 2006) and retained rather stable signal contributions over the SAR cycles (D_e(t) plots after Bailey, 2000). A dose recovery test (ca. 145 Gy given dose) was conducted on one sample per site to ensure adequacy of the SAR protocol and yielded Measured-to-Given dose (M/G) ratios of 1.01 ± 0.03 (RIN2) and 0.93 ± 0.04 (RINI4-1) for pre-heat temperatures of 240 °C (Table S5). This temperature was previously found to be suitable for the RIN sample-set (Mueller et al., 2020). An IR depletion ratio step was implemented at the end of each sequence to check for F contamination, however, none of the aliquots of SA type 1 had to be rejected on this account (IR depletion >20%). Recuperation, recycling and DRC fitting (Table S4) were of no concern allowing, for the application of the SGC approach for this SA type. Fitting of an LS normalised SGC was applied to measurements of RINI4-1 (Fig. S4) following Mueller and Preusser (2022). A signal growth ratio (SGR) was determined for the two highest, sensitivity-corrected, regenerative doses (ca. 700 Gy and 1100 Gy) to determine whether a comparable behaviour is present in the DRC (Li et al., 2016). The SGRs of RINI4-1 are between 0.96 and 1.08 and yield a CAM of 1.03 ± 0.01. The overdispersion (OD) is consistent with 0% and separated populations of the SGR is not present. A rather small scatter in SGR of less than 13% difference between the aliquots of the sample is observed. This is lower than what has been reported previously for the region (RIN sample-set; ca. 30%; Mueller and Preusser, 2022) and significantly lower than a difference of about 200% for SG Q measurements (Hu et al., 2019, 2020; Fu et al., 2020) or about 90% for small Q aliquot measurements (Li et al., 2016) that has been described for other sites. Hence, the presented DRCs here are regarded uniform and a distinction into different DRC groups is redundant, in contrast to previous findings.

Dose recovery test measurements were re-normalised and projected onto the SGC, and through this, M/G ratios of the common SAR approach could be reproduced within uncertainty (1 σ; 1.00 ± 0.05). D_e values obtained using the SAR DRC in comparison to the SGC approach (Fig. S5 A.) achieve an R^2 value of 0.84. The average fitting error is below 0.02 and an FOM value of 5.3% is observed (Table S2). The latter is well below the recommended 10% (Peng and Li, 2017) confirming the suitability of the SGC fits.

In comparison, SA type 2 presented a substantial response to the IR depletion step within the full SAR measurements. This required the implementation of an IR screening step (50 s, 850 nm) prior to any measurement and disqualified the application of the SGC approach for these samples measured following the full SAR protocol (Table 1). An extensive screening of HABS1-3 (80 aliquots), GBR1 (380 aliquots) and UST 1 (349 aliquots) allowed for the measurement of 51, 108 and 36 aliquots, respectively. However, the aberrant shape of SA type 2 decay signals (Fig. 4B–D) demanded the assessment of signal component contribution. In comparison to SA type 1, the decay signals are rather dim and show low contributions of the fast component (<80%) or change of component composition between natural and regenerative dose measurements, which is expressed in inconsistencies in the D_e(t)-plots (Bailey, 2000). To ensure that aliquots inheriting SA type 2 characteristics were excluded from any further assessment, component composition was implemented as a rejection criteria (fast component >80%). This criteria was applied consequently to both SA type 2 and 1 OSL measurements prior to the application of any other rejection criteria (see section 3.3). Due to this criterion, between 33% and 81% of full SAR measurements had to be excluded from D_e determination (Table S4). For UST1, only 7 out of the 349 aliquots initially screened passed the rejection criteria, which is regarded as statistically insufficient for a

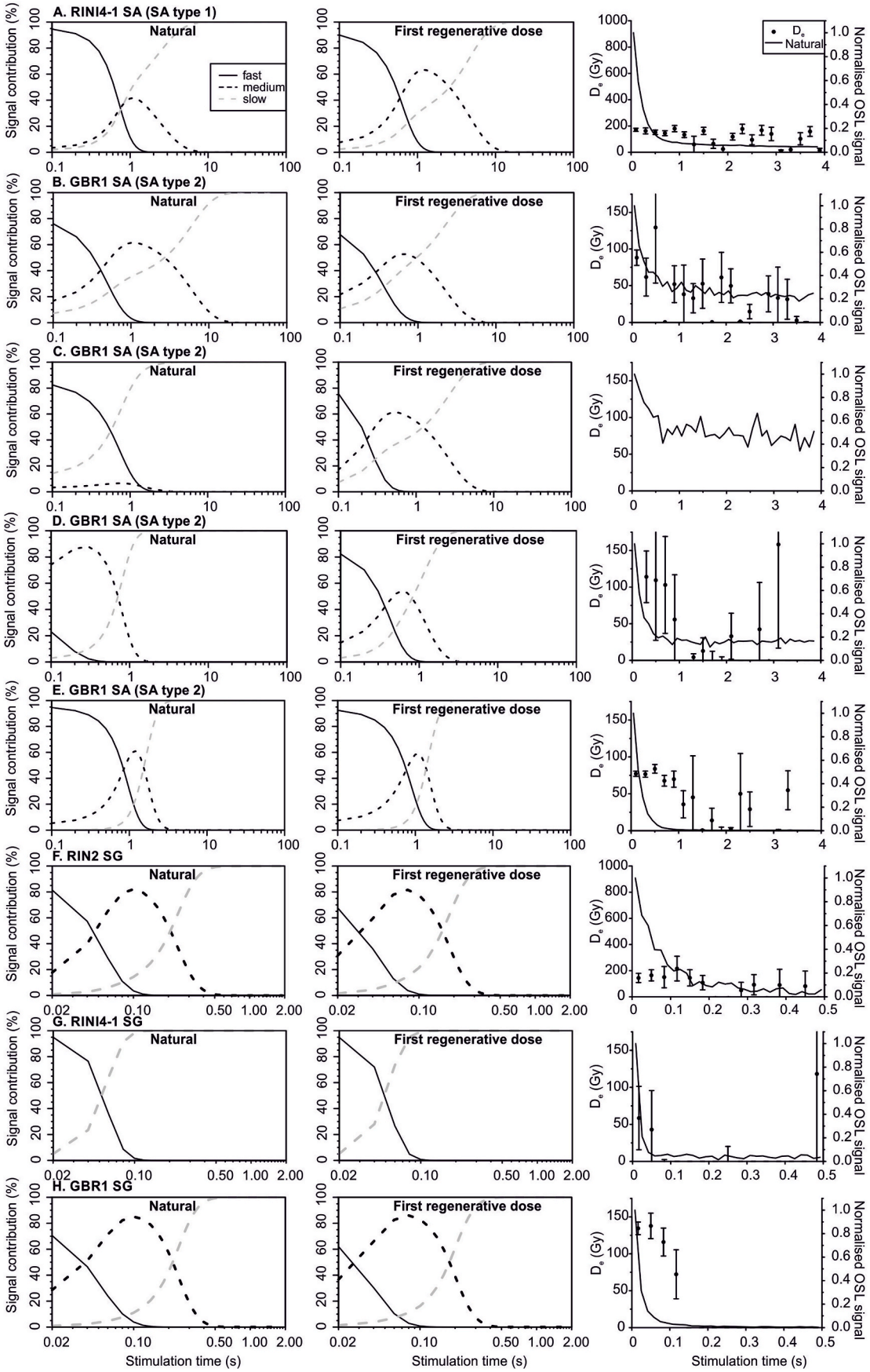

Fig. 4. Deconvoluted SA and SG OSL signals for different samples. D_e(t)-plots show D_e values for the initial signals deriving using two channels as well as the normalised OSL signal. Note, missing D_e values in the D_e(t) plots are due to limitations of the calculation software.

finite D_e determination. Due to the lack of material and its characteristics, any further Q measurements for site UST were subsequently abandoned. In contrast, 36 out of 380 initially screened aliquots were acceptable (Fig. 4E) for GBR1 allowing for a finite D_e determination, however, it was refrained from measuring further samples of this site.

For SA type 2, M/G ratios of the dose recovery tests result of 0.98 ± 0.03 (GBR1) and 0.97 ± 0.08 (HABS1-3) were obtained. Only one SA of GBR1 had to be rejected due to IR depletion issues during D_e determination (Table S4). While DRCs were all well fitted with the double-saturating exponential function, they present a wide spread of non-uniform shapes (Fig. S4) validating the dismissal of the SGC approach for these samples. Lifetime measurements were conducted on SA type 2 (RINI4-1) and type 1 (GBR1, HABS1-3) samples following Murray and Wintle (1999), as previously used with success on comparable samples of the region (e.g. Lowick et al., 2010, 2015; Buechi et al., 2018). However, Q signal intensity of the investigated samples was too low to achieve useable results.

Both HST samples represent a third type of Q (SA type 3). Initial testing of these samples showed significantly low signal intensity, IR depletion and recycling issues. Hence, further measurements of this Q fraction were suspended.

4.2. Signal properties of SG quartz

For all SA type 1 samples (RIN2, RIN4, RINI4-1; see 4.1), SG dose recovery tests were conducted yielding M/G ratios between 0.96 ± 0.04 and 1.07 ± 0.04 (Table S5) thereby confirming the suitability of the measurement protocol used (Table 1). However, SG D_e measurements of all three samples showed rather dim signals with low signal to background ratios (example for RIN2 and RINI4-1 in Fig. 4F and G). For both, RIN2 and RIN4, D_e values derived from different initial signal integrals (D_e(t) plots; example in Fig. 4) show consistent values for the majority of

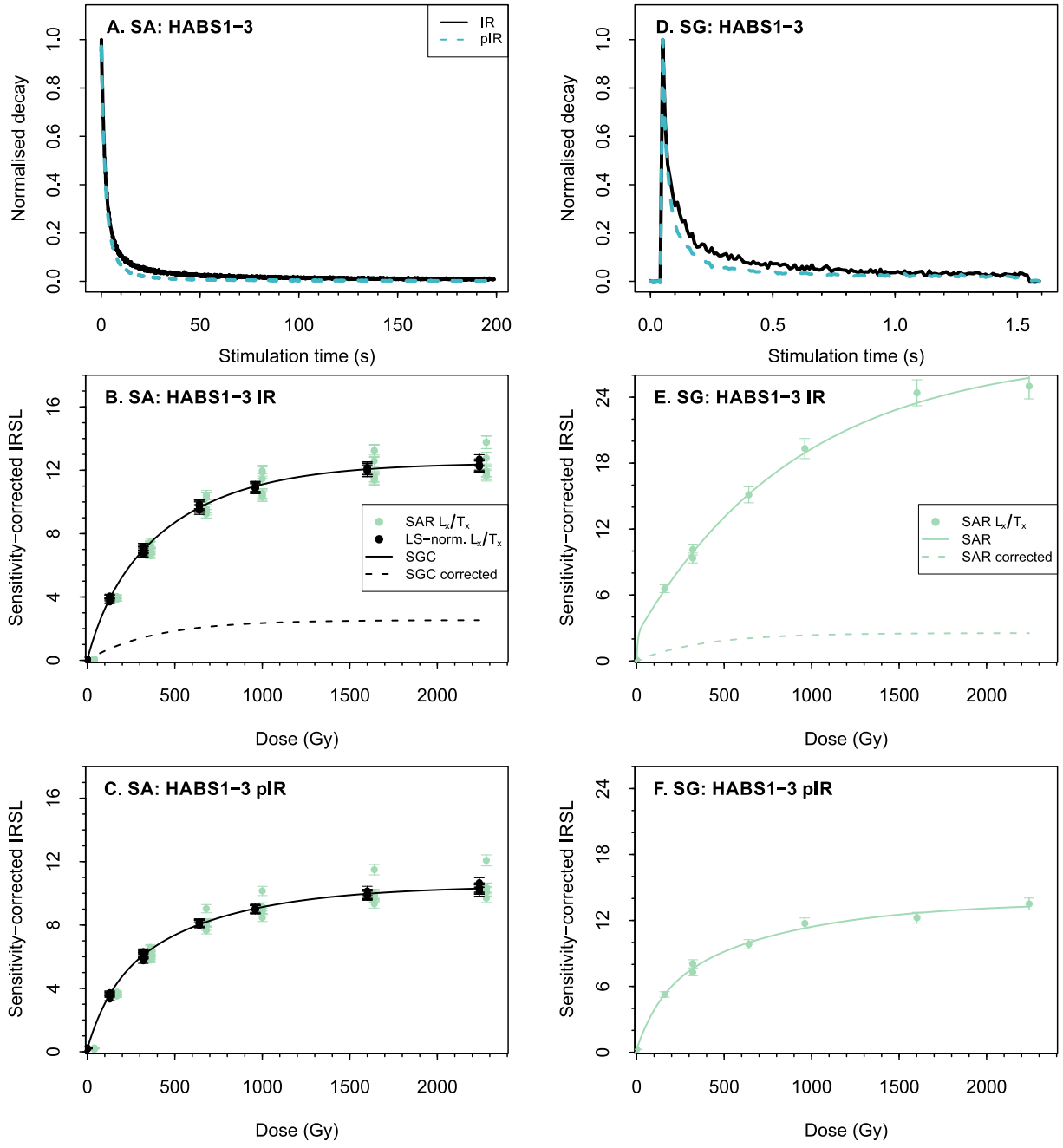

Fig. 5. *Representative examples of IR and pIR normalised decay and DRC or SGC. SA measurements (**A** to **C**) and SG measurements (**D** to **F**) are shown for HABS1-3.*

the measured decay duration. However, neither the natural nor the regenerative signals of these samples appeared to be dominated by the fast component, which contrasts observations of SA measurements. The absence of a dominant fast component in the deconvoluted signal may well be due to the rather dim nature of the signal. For RINI4-1, the measured signals were comparatively bright and showed a similar shape to the SA measurements (Fig. 4A and G). However, only two components can be derived mathematically with clear dominance of the fast component. This allows to determine consistent D_e values over the initial decay (<0.1 s). In agreement with SA results, only few grains from all three samples showed IR depletion, recuperation or recycling issues, while the majority of grains were rejected for dimness (73%–82%) or for dose response points unsuitable for curve fitting (13%–15%; Table S4). While 1500 (RIN2, RIN4) and 6500 (RINI4-1) grains were measured, only about 3% and less than 1% of the grains, respectively, gave acceptable D_e values.

For SA type 2 samples, SG measurements of UST1 were abandoned due to yielding a statistically inadequate number of finite SA D_e values. Sample material of HABS1-3 however was insufficient to conduct SG measurements. For GBR1, a M/G dose ratio of 0.94 ± 0.05 was obtained by the dose recovery test and 6500 grains were measured for D_e determination. In contrast to the SA measurements, only about 3% of the 6500 measured grains suffered from IR depletion, while most grains (82%) were rejected for dim signal characteristics. Similar to the accepted SA measurements (Fig. 4E and H), grains of GBR1 showed a comparatively bright signals that allowed for the determination of consistent D_e values over the initial decay (<0.1 s). However, SG measurements showed a reduction of fast component contribution between natural and regenerative dose signals. Less than 1% of the SG measurements were accepted, while about 10% of SA measurements passed the rejection criteria.

4.3. Signal properties of SA feldspar

In contrast to Q, the natural decay of the SA F signals (IR, pIR) were very bright and the normalised shapes were well reproducible (example in Fig. 5). As previously reported for Swiss F samples (Mueller et al., 2020), only few grains emitted an effective, bright, natural luminescence signal. This is also applicable to samples of this study, however, 1 mm aliquots (ca. 10 grains) emitted sufficient signal to oversaturate the photomultiplier tubes Therefore, a cardboard barrier (Lexsyg Research; Mueller et al., 2020) and a Schott NG4 1.2 mm glass filter (400–700 nm transmission; Lexsyg Smart) had to be used to prevent oversaturation.

SA dose recovery tests were conducted on at least one sample per site (Table S5) for given doses of ca. 145 Gy and a preheat temperature of 250 °C. M/G ratios of the IR signal yielded between 0.92 ± 0.03 (HABS1-3) and 1.04 ± 0.05 (RINI4-1) and between 0.98 ± 0.03 (HABS1-3) and 1.03 ± 0.03 (RIN4) for the pIR signal.

For both the IR and pIR signals, 3%–17% of aliquots for samples HST15, RINI4-1 and UST3 presented signals in saturation and were rejected. However, the majority of measured SA passed rejection criteria (i.e. DRC fitting, recuperation and recycling tests; Table S4) and were consequently included into D_e determination. LS-normalised SGCs were fitted to all samples, with representative examples shown for sample HABS1-3 in Fig. 5. Average errors ≤0.07 and FOM values of between 1.2% and 5.2% were obtained, with the latter complying to the recommended range.

After re-normalisation and projection onto the SGC, dose recovery test results reproducing those of the common SAR approach are obtained within uncertainty (1 σ) for both IR and pIR signals (Table S2). When comparing SAR derived D_e values with those derived using the SGC (Fig. S5 B.), R^2 values of close to 1 are determined for most samples. However, some samples showed lower R^2 values especially for the pIR signal in comparison to the IR signal. Neither of the samples showed a systematic over- or underestimation of D_e values when using either the SAR or the SGC. Hence, the observed discrepancies are likely due to an amplification effect of D_e differences that occurs in the high dose range of the fitting curves. One exception was UST1, for this sample a R^2 value of 1.00 is obtained for the pIR signals, while only 0.11 is reported for the IR_{50} signals. This is solely due to one outlier that had significant impact as only a small number of measurements were conducted (n = 7). As a means of verifying the application of the SGC approach, R^2 is limited in its use, however, the observed fitting parameter justifies the application of the SGC.

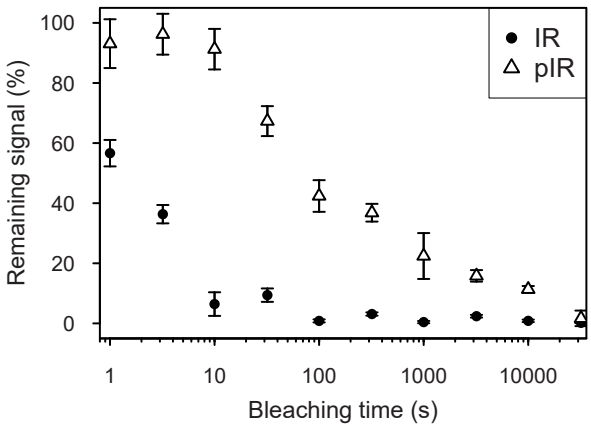

Fig. 6. Natural D_e values (IR and pIR) measured after 900 s of IR LED light or seven days of sunlight exposure. Each measurement value represent the CAM D_e value for three SA.

4.4. Bleaching behaviour of SA feldspar

Two SA bleaching experiments were conducted to investigate the bleaching behaviour (1) for different light sources and (2) for the different luminescence signals (IR, pIR).

The first experiment (1) was conducted on two samples by exposing three aliquots of each sample to either 900 s of IR LED light or seven days of sunlight (Freiburg, Germany; 48°00′N 7°50′E; April 2021). Both light sources sufficiently reset the IR signal with residuals below 3 Gy (Fig. 6). Similarly, the residuals of the LED bleached pIR signals were below 4 Gy, while those of the sunlight bleached pIR signals accounted for up to about 12 Gy. Sample GBR1, with the lowest natural dose (ca. 70 Gy), retained the lowest residual while RINI4-1 with natural doses an order of magnitude higher, presented residuals about twice as high suggesting that residual doses increase with the natural doses. This and the amount

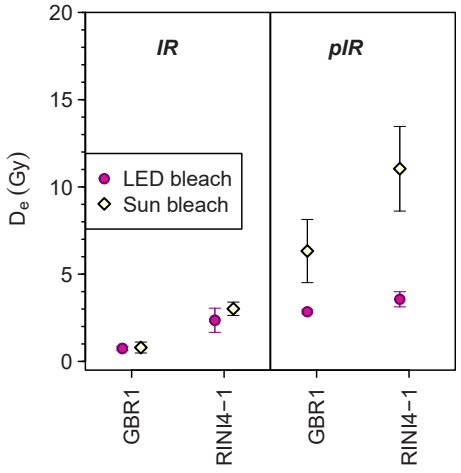

Fig. 7. Remaining IR and pIR D_e values after LED bleaching for a given dose of 145 Gy. Results shown here are representative for all measured samples and were conducted on one, previously sensitised aliquot of RINI4-1.

of the residual doses agree well with previously reported observations (cf. Zhang and Li, 2020). The observed residuals are negligible in comparison to the natural doses of the measured samples in this study, therefore, no subtraction was conducted.

To compare the bleaching behaviour of the two different luminescence signals (2), three samples (GBR1, HABS1-3, RINI4-1) were chosen. One sensitised aliquot per sample was repeatedly given a dose of 145 Gy followed by an IR and pIR measurement using the same protocol as used for D_e determination (Table 1). During each repletion, the dose was recovered after different times of exposure (1 s, 3.2 s, 10 s, 32 s, 100 s, 320 s, 1000 s, 3200 s, 10000 s, 32000 s) to the build-in solar simulator in the Lexsyg Research (Øλ: 365 nm with 10 mW; 462 with 63 mW; 525 nm with 50 mW; 590 nm with 37 mW; 625 nm with 115 mW; 850 nm with 96 mW). After 1 s of solar simulattion, less than 60% of the initial IR signal are left while about 95% of the IR signal was bleached after 10 s (Fig. 7). For the pIR signal, after 10 s of solar stimulation about 90% of the signal still remained while it takes almost 9 h (32000 s) of exposure to the solar simulator to reduce the signal close to 0%. Similar results were shown by Preusser et al. (2021).

4.5. Anomalous fading of SA feldspar

For F, SA fading tests were conducted on both Lexsyg and Risø readers following Auclair et al. (2003). Fading parameters were determined for three aliquots of representative samples from each site (Table S6). Therefore, aliquots previously used for D_e determination or dose recovery tests were given a dose of about 145 Gy and a subsequent test dose of ca. 25 Gy. On the Risø, storage times of ca. 0 s, 2.5 h, 5 h, 40 h and up to 300 h were applied, while a shortened protocol was used on the Lexsyg. For this, the given dose was measured after ca. 0 s, 1 h, 2.5 h, 5 h and 10 h, with three cycles of these storage times being implemented per aliquot. With this, the aliquot remained on the sample arm constantly to reduce the possibility of sample material being lost during mechanical transfer of the aliquot between the sample arm and the storage carousel (Preusser et al., 2014).

For comparison, the decadal percentages of signal loss (g-value) normalised to 2 days (Lamothe et al., 2003) were calculated for the IR and pIR signals (Fig. 8; Table S6). For the IR signal, g-values (in % per decade) determined with both readers fall into the same range with 1.0 ± 0.7 (RIN4) to 3.1 ± 0.9 (UST1) on the Lexsyg and 1.9 ± 0.4 (RIN2) to 3.2 ± 0.4 (GBR1) on the Risø. However, IR g-values of the individual samples vary notably ($R^2 < 0.01$) without a systematic difference. The g-values for the IR signal are very similar to those obtained in previous

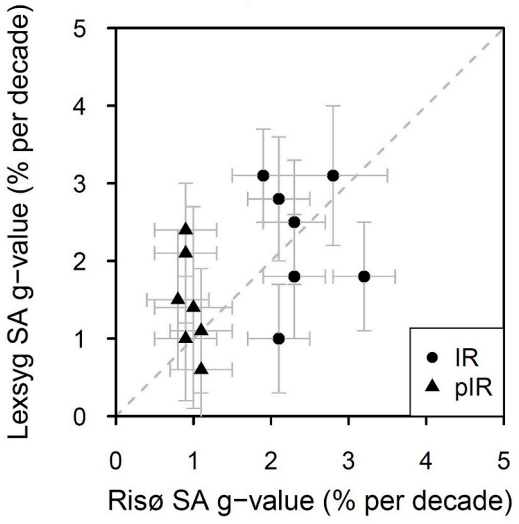

Fig. 8. SA fading values obtained using two different readers. Each g-value represent the CAM value for three SA.

studies on the region (Dehnert et al., 2012; Gaar and Preusser, 2012; Lowick et al., 2012, 2015; Gaar et al., 2013; Buechi et al., 2017; Mueller et al., 2020). While it has been common to refrained from applying a fading correction for samples of the region in previous studies, Gaar et al. (2013) and Mueller et al. (2020) have demonstrated the necessity of such a correction by presenting corrected F ages in good agreement with those of Q.

To derive fading corrected SA D_e values, the sample specific density of recombination centres (ρ'-value) was determined and then used to correct the SGC or DRC following Kars et al. (2008), using the Luminescence package for R (King and Burow, 2019). For the Lexsyg, SA IR ρ'-values between $8.17e^{-7} \pm 3.29e^{-7}$ (RIN4) and $2.49e^{-6} \pm 8.46e^{-7}$ (RIN2) were derived, while SA IR ρ'-values for the Risø ranged between $1.55e^{-6} \pm 2.42e^{-7}$ (RINI4-1) and $2.20e^{-6} \pm 5.89e^{-7}$ (GBR1) (Table S6).

In contrast to the IR signals, the SA pIR g-values showed a systematic difference with values obtained on the Risø falling in a much smaller range with 0.8 ± 0.4 (HABS1-3) to 1.1 ± 0.4 (HST2, RIN4) than those of the Lexsyg with 0.6 ± 0.8 (HST2) to 2.4 ± 0.6 (RIN2). Thiel et al. (2011a, b) found for a higher temperature protocol (pIR_{290}) that g-values of up to 1.6 are likely laboratory artefacts. Correspondingly, Buylaert et al. (2012) observed comparable values for fading measurements of Q and suggested that g-values up to 1.5 originate from measurement procedures rather than represent a fading signal. These thresholds are similar to most of the pIR g-values obtained here. However, when the fading correction is applied to the pIR signal, most samples reach saturation (data not shown), thereby hindering the interpretation of the observed signals. To allow for comparison between the IR and pIR signals, the uncorrected pIR signal is used in this work.

Note, all SA F D_e distributions presented in this study may be impacted by aliquot specific variations in fading rates, as no fading correction was conducted for the SA pIR signals and a sample specific averaged fading rate was used for IR_{corr}.

4.6. Signal properties of SG feldspar

In comparison to the SA measurements, the natural decay signals of SG F (IR, pIR) are somewhat dimmer, posing no risk of oversaturating the photomultiplier tube. However, the signal to background ratios are sufficiently high and the normalised decay shapes are well reproducible (example in Fig. 5). Between 36% (HABS1-3) to 83% (UST1) and 46% (HABS1-3) to 84% (UST1) of the grains failed to present an effective, bright, natural IR or pIR signal, respectively. Those grains were rejected, together with up to 13% of grains for recycling, 26% for recuperation and 3% for fitting problems. In addition, for most samples up to 1% of grains were rejected due to saturation of the IR and pIR signals. Four samples presented higher percentages of saturated pIR signals with 3% (GBR1, HABS1-3), 8% (HST15) and 13% (RINI4-1) of the measured grains being excluded from D_e determination (Table S4).

The suitability of the SG measurement protocol was assured with dose recovery tests for eight samples yielding M/G ratios of the IR signal between 0.93 ± 0.02 (RINI4-1) and 0.97 ± 0.02 (GBR1, UST1, HABS1-3) and between 0.96 ± 0.0 (GBR1) and 1.03 ± 0.02 (UST1) for the pIR signal (Table S5).

4.7. Signal brightness of SG feldspar

Several studies have reported a positive correlation between the luminescence signal intensity obtained for a given dose from grains and their natural D_e values (Reimann et al., 2012; Smedley, 2014; Brown et al., 2015; Rhodes, 2015; Jacobs et al., 2019; Guo et al., 2020), suggesting that only the brightest grains of a population provide reliable D_e values. Following Jacobs et al. (2019), this relationship has been assessed for all accepted SG IR and pIR measurements of this study. For this, CAM D_e values were derived using all grains below given T_n thresholds (initial cts/0.6 s; Fig. 9 and S6) for both the measurement of the natural signal and also for the dose recovery tests (when applicable).

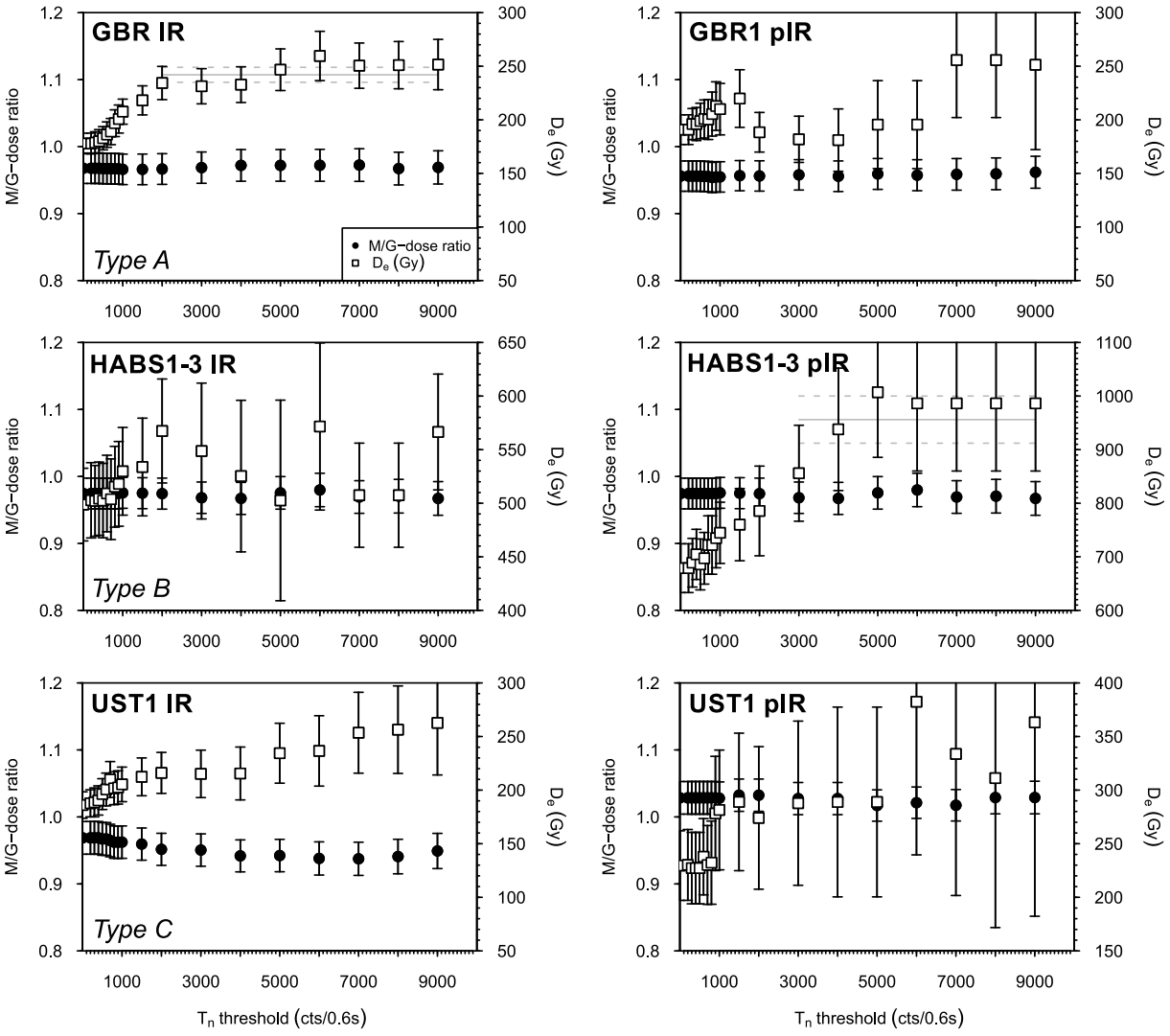

Fig. 9. T_n threshold plateau determination for all types shown on representative examples. CAM D_e values for the natural signal and dose recovery test results are presented as a function of signal brightness or intensity (cts/0.2 s). Note, distinct plateaus are observed for the IR signal of type A and the pIR signal of type B.

For the latter, all samples showed D_e values over the entire range of investigated thresholds that are consistent with each other suggesting that a given dose can be recovered regardless of the signal intensity of the grains. In contrast, for the natural signal, three types of relationships were observed; type A is characterised by IR D_e values that increase with the applied T_n thresholds until a plateau is reached, while no such relationship is present in the pIR signal (GBR1, HST2, RIN2, RIN4); for type B such a relationship is present in the pIR measurements but is missing for the IR signal (HABS1-3, UST3), while type C lacks any correlation between signal intensity and D_e values (GBR12, HST15, RINI4-1, UST1). For types A and B, the onset of the plateau is used to determine a sample specific T_n threshold that will allow for the exclusion of grains likely to underestimate the D_e distribution. Hence, sample specific thresholds (2000–3000 cts/0.6 s) have been determined for either the IR (type A) or the pIR signal (type B) and the D_e distributions have been "cleaned" from dim grains. This significantly reduces the number of grains acceptable for final D_e determination by 68%–70% (Table S7).

However, in the absence of such a relationship it might well be advantageous to exclude dim grains following previously established relationships. Reimann et al. (2012) suggested selecting the brightest 30% of grains which is similar to results obtained using the T_n threshold in this study. Hence, only the D_e values of 30% of the brightest grains were chosen for each sample of both the IR and pIR signals for further discussion (see 5 and 6.2).

As only the natural signal appears to have a link between signal intensity and obtained D_e value, anomalous fading of the natural signal should be assessed for the individual grains rather than for multi grain aliquots, as previously presented and commonly used for fading correction (see 4.5).

4.8. Anomalous fading of SG feldspar

To further investigate fading, five samples were chosen (GBR1, HABS1-3, RIN2, RINI4-1, UST1) for which SG D_e values were determined. Subsequently SG fading measurements were conducted on the same grains following the same procedure as for SA measurements (Risø reader; see 4.5). SG IR g-values (% per decade) plot between -2.60 ± 2.38 and 13.86 ± 3.82, while pIR g-values scatter between -4.65 ± 3.18 to 5.01 ± 2.33 (Fig. 10A and B). The wide spread observed for SG IR g-values is only reported for grains with natural D_e values below 150 Gy.

When plotted against signal intensity (Fig. 10C and D), it becomes obvious that grains with low IR intensity are more likely to present a wider scatter of g-values. This is especially true for grains with an intensity below 2000 cts/0.6 s, with a further reduction of scatter above

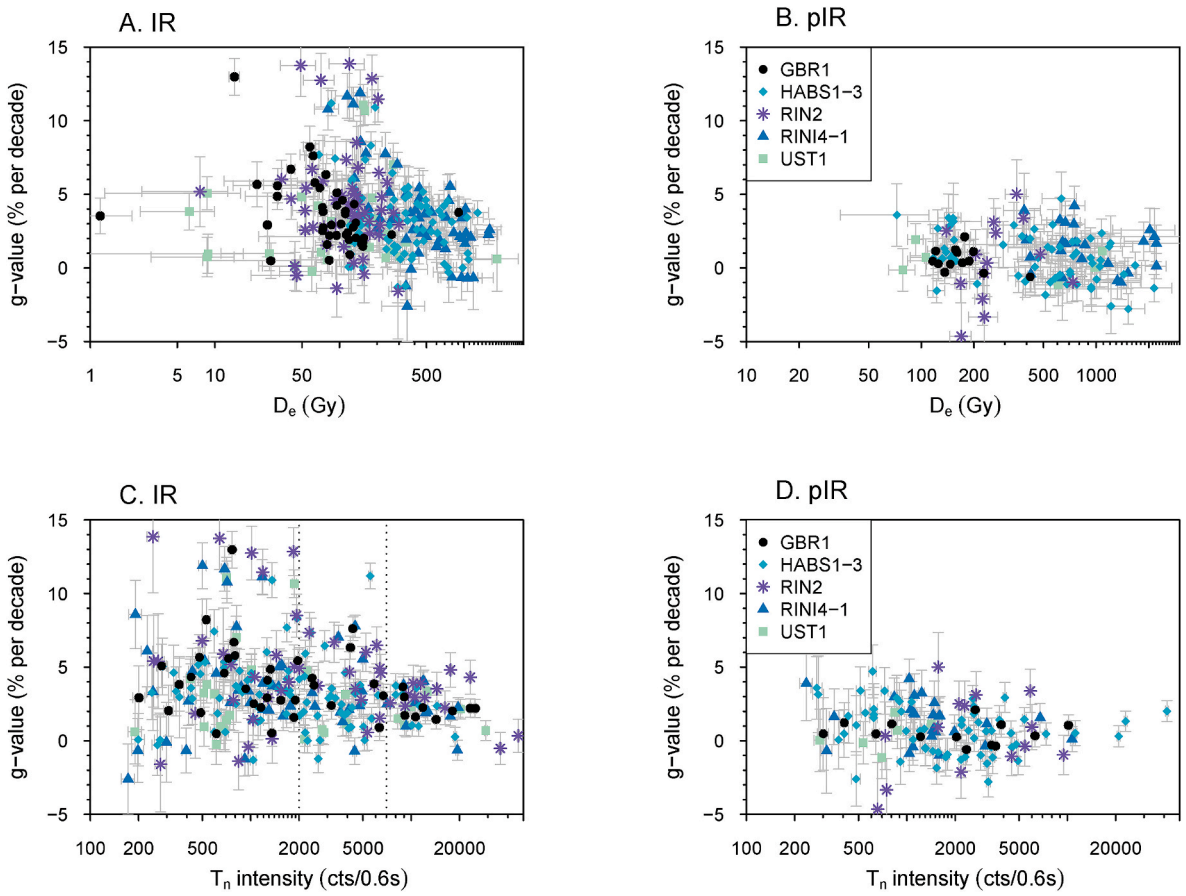

Fig. 10. IR and pIR SG g-values as obtained for five samples and plotted against D_e value and signal intensity of the individual gains. The dotted lines (C.) indicate a change in g-value spread (see text for further details).

7000 cts/0.6 s, suggesting that fading rates of individual grains vary significantly. Sample specific T_n thresholds of 2000 cts/0.6 s as determined previously for type A samples (GBR1 and RIN2; see 4.7) agree well with this observation and justify the exclusion of grains with dim IR signals as proposed. Type B sample HABS1-3 and type C samples RINI4-1 and UST1 lacked an IR D_e plateau that allows for the application of the T_n threshold approach, however, SG g-values of these samples show a similar pattern to those of type A. A dependency of D_e values to individual fading rates would be expected when deriving CAM D_e values for different signal intensities. In addition, a relationship between signal intensity and g-values is missing for the pIR signal of HABS1-3 (type B), while this sample presents a T_n threshold plateau. This is in accordance with findings of Rhodes (2015) for a SG pIR short-term fading experiment on samples from California and both IR and pIR g-values for samples from New Zealand observed by Smedley (2014). For IR measurements of samples from Saudi Arabia, Trauerstein et al. (2012) found a similarly wide scatter of SG g-values for grains with lower D_e and brightness. However, they observed a negative correlation between those parameters, a dependency not observed in samples investigated here. Whether there factually is no such relationship or whether it may be masked by other factors attributing to the D_e distribution pattern will be discussed below (see section 6.2). Note, all SG F D_e distributions presented in this study may be impacted by grain specific variations in fading rates as no fading correction was conducted for the SG pIR signals and a sample specific averaged fading rate was used for IR_{corr}.

5. Results

All SA and SG D_e values and distributions are presented in Table S3 and Figure S7, respectively. Representative D_e distributions are shown in Fig. 11. To further assess the spread of D_e value for each signal, individual D_e values were normalised to the signal's CAM D_e value (Fig. 11). DRC and SGC saturation values are provided in Tables S4 and S8. All apparent ages are given in Table S9 and discussed below for comparison between the Q and F results. For further discussion, selected apparent ages are presented together with the sedimentological logs in Fig. 2. How to interpret the MAM apparent ages derived for F will be discussed in section 6.2.

5.1. Lower Aare Valley

5.1.1. Sample: GBR1

For the sample expected to be the youngest, GBR1, none of the measured aliquots were saturated or close to $2*D_0$ (86% saturation) of the signal-respective SGC. D_e distributions of all signals, IR_{corr}, uncorrected pIR and OSL, show a very similar, almost normally distributed shape with few outliers in the high D_e value range. This is reflected by OD values between 33% and 47%. After outlier analysis using nMAD, the nMAD CAM yielded OD values $\leq$ 25% and D_e values of 82 $\pm$ 4 Gy (OSL), 128 $\pm$ 4 Gy (IR_{corr}) and 148 $\pm$ 5 Gy (pIR). The OSL apparent age of 64 $\pm$ 4 ka and the IR_{corr} apparent age of 61 $\pm$ 3 ka are statistically consistent with each other. In comparison to OSL, a slightly higher apparent age of 70 $\pm$ 4 ka was obtained from the pIR signal. This may either be due to the exclusion of few low pIR D_e values with small uncertainties when applying the nMAD, a small residual that was retained even after sufficient sunlight exposure (on average about 6 $\pm$ 2 Gy; see section 4.4) or a combination of both. However, it is unlikely that the pIR signal suffers from a higher degree of partial bleaching than the OSL signal, as both show almost identical shape of D_e distributions. This, the similarity in D_e distribution shape of all measured signals and the

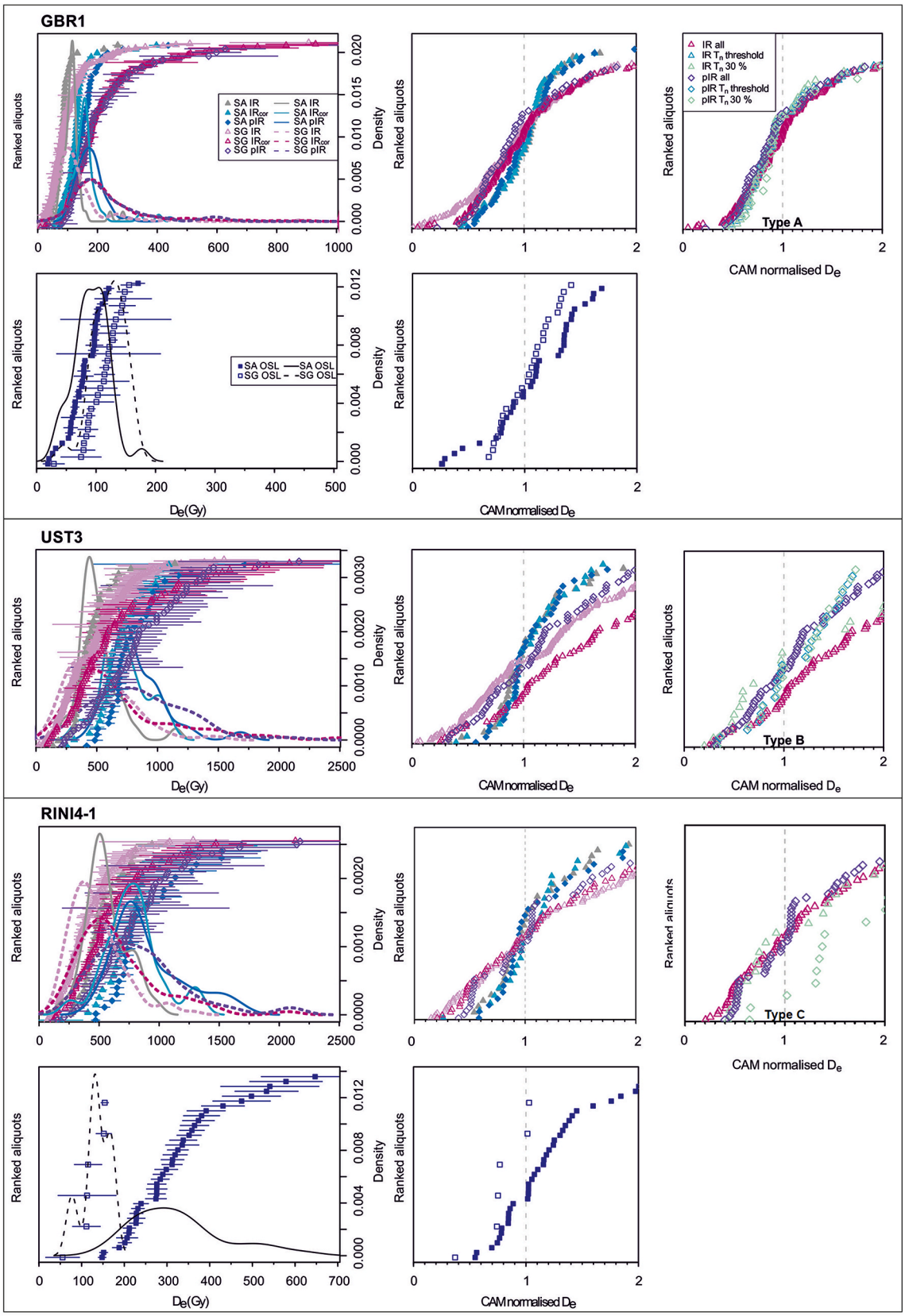

Fig. 11. (Previous page) D_e distributions (point signature) of three representative investigated samples (ranked by increasing D_e value) and signals (left) superimposed on Kernel density estimates (line signature). For the main population of each signal, individual D_e values were normalised to the signal's CAM D_e value (middle) and for further investigation of the SG signals those distributions are presented again after T_n threshold or 30% brightest grain cleaning.

consistency between OSL and IR_{corr} apparent ages suggests that all luminescence signals were bleached equally well. A SA apparent depositional age of between 61 ± 3 ka and of 64 ± 4 ka would therefore be regarded reliable for GBR1.

In comparison to the SA measurements, only the Q SG D_e distribution of GBR1 shows an almost normally distributed shape with a single outlier in the low D_e value range. Noteworthy is the significantly lower OD value (19%) of the SG distribution, in comparison to that of the SA (47%). After the exclusion of the outlier, a SG CAM D_e value of 111 ± 6 Gy and an apparent age of 86 ± 1 ka were obtained. While about 90% of all SA measurements were excluded following IR screening and the check for fast component dominance, the remaining SA still presented a variety of grains, likely including those with unfavourable properties that will have contributed to the averaged D_e value of each or most SA measurements. With less than 1% of the SG measurements accepted, the higher SG Q age (86 ± 1 ka) compared to SA (64 ± 4 ka) might indicate the successful rejection of grains with unfavourable luminescence properties from the SG dataset.

The GBR1 SG D_e distributions of IR and pIR are positively skewed and presented a rather wide spread with OD values 66% and 48%, respectively. Only few grains (three) failed to intercept with the pIR DRCs, while for 22 out of the 166 grains the IR signals were unsuccessful in reaching the DRC due to the signals being in saturation after correction. The majority of natural D_e measurements were projected onto the DRCs below $2*D_0$, with only few grains of both signals plotting above. The SG pIR and IR_{corr} D_e distributions showed near identical shapes suggesting that fading correction might have been successful and that bleaching was equally inefficient for both signals. A clear tail of D_e values is observed at the higher D_e ranges indicating pattern of typical partially bleached distributions warranting the use of the MAM (Arnold et al., 2007). However, for the SG IR signal of GBR1, a dependency between signal intensity and D_e values (type A), as well as g-values (see sections 4.7 and 4.8), was observed. Therefore, MAM D_e values were derived for the 30% brightest grains and after applying the sample specific T_n threshold yielding 188 ± 19 Gy and 193 ± 15 Gy, respectively. These values convert to SG IR apparent ages of 89 ± 10 ka and 91 ± 8 ka, which are both statistically consistent with the SG nMAD Q apparent age of 86 ± 1 ka. Both SG IR ages were derived using the MAM, which has seemingly isolated the well bleached population of the D_e distributions and hence provides rather a finite than a minimum age estimate. The SG IR apparent ages are higher than that obtained using SA (61 ± 3 ka; nMAD CAM), which was obtained from a mixture of grains including those with less intense signals.

For the SG pIR signal a MAM D_e value of 155 ± 17 Gy and an apparent age of 73 ± 9 ka were derived. The pIR age is slightly younger but statistically consistent with those of the other SG signals. In comparison, the SA pIR apparent age of 70 ± 4 ka agrees with the SG apparent age, however, it was found to be higher than the Q and IR SA age estimates. The rather high SA apparent age represents an averaged signal with contributions of grains that likely have been rejected during the SG analysis or were partially bleached. When only the brightest 30% of grains are used, a pIR MAM D_e value of 165 ± 31 Gy and an apparent age of 78 ± 15 ka can be obtained. However, the used bright grains still yield low D_e values and this cleaning step remains without impact onto the shape of the lower D_e distribution. Consequently, the consistent shape of the D_e distribution and the fact that the SG pIR apparent age of the brightest 30% of grains is statistically consistent with the pIR, OSL and IR_{corr} SG apparent ages, suggests that the rejection of dimmer grains for signals lacking a T_n threshold plateau is redundant.

Considering the consistency of the SG ages and the opportunity to exclude grains with unfavourable luminescence behaviours (i.e. dim IR signal, lacking fast component of OSL) during the analysis, a depositional age of between 73 ± 9 ka and 89 ± 10 ka may be regarded more reliable than the apparent ages derived using the SA dataset (61 ± 3 ka to 64 ± 4 ka).

5.1.2. Sample: UST1

For the second young sample, UST1, OSL measurements were unfeasible (see section 4.1). However, the SA IR D_e values are close to normally distributed with only few outliers in the high D_e range (25% OD). After outlier analysis, an IR_{corr} nMAD CAM D_e of 159 ± 6 Gy and an age of 77 ± 5 ka were derived. Similarly, the application of the MAM provides a D_e value of 148 ± 13 Gy and an age of 72 ± 7 ka. These values are statistically consistent with those of the CAM, implying that the small impact outliers have on this particular population and any impact of a partially bleached component is negligible, if present. In comparison, the pIR D_e distribution is much wider and positively skewed with some very high D_e values. This points towards a different, poorer degree of bleaching degree for this signal. However, an apparent MAM age of 79 ± 10 ka for the pIR signal is statistically consistent with that of the IR_{corr}, indicating that the lowest part of the population may represent a well-bleached component. Noteworthy, for this comparatively young sample none of the signals are close to being affected by saturation limitations.

Similar to GBR1, the SG IR and pIR D_e distributions of the second youngest sample, UST1, are positively skewed, show wider distributions (OD >60%) and a tail of D_e values towards the high range, with few D_e values yielding higher values than $2*D_0$ (IR_{corr}: 6; pIR: 15). In absence of a T_n threshold plateau (type C), IR_{corr} MAM D_e values of 115 ± 9 Gy and 147 ± 19 Gy were derived using the entire D_e population and 30% of brightest grains, respectively. This equates to MAM apparent ages of 56 ± 5 ka and 72 ± 10 ka. The SG IR_{corr} MAM apparent age derived using the brightest grains agrees well with those obtained for SA (IR_{corr} nMAD CAM 77 ± 5 ka and pIR MAM 79 ± 10 ka).

A SG pIR MAM D_e value of 98 ± 17 Gy was derived for all accepted grains and 91 ± 25 Gy was obtained for the 30% brightest grains. The rejection of dim grains reduces the number of accepted grains from 48 to 14 and increases the OD from 95% to 109%. Both approaches lead to apparent MAM ages of 48 ± 9 ka and 44 ± 12 ka, respectively, which are statistically consistent with for the MAM of the entire D_e population of the IR signal. This in turn strengthen the implication drawn from the IR dataset, that the application of a brightness cleaning step is inappropriate in the absence of a T_n threshold plateau.

Based on the poor signal performance of the younger samples from the GBR and UST sites, further OSL measurements (Q) were omitted for the two older samples (GBR12, UST3).

5.1.3. Sample: GBR12

The D_e values of the IR signals (corrected and uncorrected) for GBR12 yield an OD value below 20% and are narrowly distributed with only two outliers; one in the lower and one in the upper range. CAM and nMAD CAM D_e values are statistically consistent with each other implying that the outliers have little influence onto the average. The shapes of the distributions are almost identical to those of GBR1. While IR D_e values of GBR12 are well below saturation constrains, most of the pIR D_e values plot above 90% saturation. Noteworthy is a small number (six) of aliquots with low D_e values suggesting the potential for two pIR populations with the lower at 659 ± 56 Gy (GBR12). This results in an apparent age of 302 ± 66 ka. However, the CAM derived age of 388 ± 79 ka for the whole population is statistically consistent with the IR_{corr} nMAD CAM age of 266 ± 54 ka suggesting that the lower population has little effect on the age derivation. This is reflected in the nearly identical CAM and MAM values for all signals.

D_e values of the SG IR signals (corrected and uncorrected) yield an OD value above 60% and present wide distributions with distinct tails in the high D_e range. This is even more pronounced in the pIR distribution with about half of the grains plotting beyond 86% or even 90% saturation. Only about 3% of pIR SG measurements and about 13% of IR_{corr} measurements, failed to intercept with the DRCs. All of the D_e distributions lack a distinct population in the low D_e range but rather present a ramp-shaped pattern. A T_n threshold plateau was found for none of the signals of GBR12 (type C), however, D_e values derived for the 30%

brightest grains and for the entire D_e population returned MAM D_e values within error of each other for the SG IR_{corr} and SG pIR measurements. This indicates that a brightness cleaning step is redundant for type C samples. MAM D_e values of 201 ± 27 Gy and 375 ± 45 Gy as well as apparent ages of 92 ± 22 ka and 172 ± 40 ka were obtained for the IR_{corr} and uncorrected pIR signals, respectively. The IR_{corr} age is thereby statistically consistent with those ages obtained for GBR1, which was collected from the same core some 80 m above GBR12 and was suspected to be of similar age. This might indicate that corrected SG IR D_e values isolated by the MAM may represent a well-bleached fraction of the sample, while the low range of SG pIR D_e values lack full bleaching.

Both SG apparent age estimates are less than half of those obtained for the SA measurements (IR_{corr} nMAD CAM 266 ± 54 ka; pIR CAM 388 ± 79 ka) suggesting that the averaged signal of the SA measurements masks partial bleaching as successfully observed for both signals in the SG measurements. This is expressed in tight SA distributions, very low OD values and equal results for the CAM and MAM.

5.1.4. Sample: UST3

For the SA pIR signal of UST3, a comparatively wide spread of D_e values is observed (OD >20%) with the majority of values being close to or above the 86% saturation marker and few aliquots fail to intersect with the respective SGC. When applying the MAM, the apparent SA pIR age of 395 ± 38 ka exceeds that of the SA IR signal (285 ± 35 ka). However, for all distributions of UST3, some D_e values (seemingly outliers) in the low range are observed limiting the applicability of the MAM.

For all signals, the SG D_e values of UST3 resemble those of GBR12 by being widely scattered and positively skewed with OD values of 71% (IR_{corr}) and 45% (pIR). About 8% of grains fail to intercept with the according DRC for the IR_{corr} signals, while this is true for about 10% of the pIR signals. About one third (IR_{corr}) or half (pIR) of the measured grains projected onto the DRCs above 86% and 90% saturation, respectively. For this sample that was likely partially bleached, a SG MAM D_e value of 185 ± 23 Gy and an apparent age of 104 ± 14 ka were derived from the whole population of the IR_{corr} signal. As a type B sample, only the pIR signal presented a T_n threshold allowing for the calculation of a MAM D_e value of 597 ± 122 Gy with an associated apparent age of 338 ± 70 ka. This is in agreement with values derived using the brightest 30% of grains (575 ± 130 Gy, 324 ± 75 ka), however, the pIR age estimate is three times higher than that of the IR_{corr} signal. Good agreement between IR_{corr} and pIR MAM estimates was obtained for UST1, collected from the same core 20 m above UST3 This indicates that a fading correction for IR can be successfully applied to samples from this site and that the discrepancies between those signals of UST3 can rather be attributed to bleaching. The shape of the pIR D_e distribution may imply that even the low range is represented by grains that were denied sufficient light exposure and that most of them still contain a residual signal. The poor bleaching was already observed in the SA dataset with outliers in the low D_e value range, which explains why even SA MAM apparent age estimates are much higher than those of the SG dataset (IR_{corr}: 285 ± 35 ka, pIR: 395 ± 38 ka).

5.2. Habsburg-Rinikerfeld Palaeochannel

For all samples from the Habsburg-Rinikerfeld Palaeochannel, SA OSL measurements could be obtained and compared to the IR results.

5.2.1. Sample: RIN2

For the first drill core sample, RIN2, none of the measured aliquots were saturated or close to the saturation limit. The D_e distributions of all signals, IR_{corr}, and uncorrected pIR and OSL, showed a very similar, almost normally distributed shape with few outliers at either the high, the low or both ends of the D_e value range. This is reflected in OD values between 19% and 25%, although, the IR_{corr} D_e distribution presented a wider spread and an OD value of 37%. After outlier analysis, the nMAD CAM yielded D_e values of 162 ± 4 Gy (OSL), 294 ± 9 Gy (IR_{corr}) and 308 ± 7 Gy (pIR). The OSL age of 190 ± 9 ka, the IR_{corr} age of 176 ± 8 ka and the pIR age of 184 ± 8 ka are statistically consistent with each other.

In comparison to the Q SA measurements of RIN2, the Q SG D_e distribution presented a more normally distributed or even spread, without distinct outliers in the upper range. This distribution had an OD value of 24% and resembled that of the well bleached sample GBR1. None of the accepted grains plotted above the $2*D_0$ saturation limit on the respective DRC. A CAM D_e value of 176 ± 8 Gy and an apparent age of 206 ± 12 ka were derived. The agreement between SG and SA OSL apparent age estimates (SA 190 ± 9 ka) strengthens the implication of a well bleached Q signal.

In contrast to the Q signal, both SG IR and pIR signals showed a somewhat broader spread of D_e values than observed for the SA measurements. A slight positive skew is present, but less so in comparison to the observations for GBR1. Only few grains (seven) of the pIR signal intercepted the respective DRCs above 86% saturation. OD values of the IR_{corr} signal (2% of grains in saturation) reached 48%, but are reduced to 29% (brightest 30% of grains) to 35% (T_n threshold) after brightness cleaning for this type A sample. These are still rather high and with few grains tending towards a high D_e value tail, representing a partially-bleached component. Therefore, MAM age estimates were derived for datasets of both the T_n threshold and the brightest 30% of grains. Both cleaning steps changed the lower part of the D_e distribution notably. MAM D_e values of 190 ± 22 Gy and 236 ± 22 Gy with the associated apparent ages of 113 ± 14 ka and 141 ± 14 ka were yielded, respectively.

Similarly, an OD value of 34% was reported for the pIR signal, with only one grain being in saturation. A pIR MAM D_e value of 255 ± 28 Gy and an apparent age of 152 ± 18 ka were derived. While the OSL ages for both the SG and SA dataset agree well, the pIR and IR_{corr} MAM ages derived using SG are comparatively low.

5.2.2. Sample: RIN4

Similarly, the second drill core sample, RIN4, presented rather tight SA distributions with accordingly low OD values (8%–21%) and only few outliers for the OSL and pIR signals. After discarding those outliers, the nMAD CAM yields SA D_e values of 212 ± 6 Gy for OSL and of 313 ± 6 Gy for pIR. Those provided statistically consistent apparent ages of 178 ± 9 ka and 168 ± 7 ka, respectively. The IR_{corr} age of 121 ± 5 ka (225 ± 3 Gy) is much lower than the apparent ages obtained for the other signals.

For RIN4, the SG Q D_e distribution resembles that of RIN2 and GBR1, with an even spread and no distinct outliers. An OD value of 14%, a CAM D_e value of 203 ± 5 Gy and a respective CAM finite age of 171 ± 8 ka were derived. This age agrees with the SA apparent age of 178 ± 9 ka suggesting a well bleached Q fraction. However, all IR (uncorrected and corrected) and pIR D_e distributions show a wide spread with a distinct tail in the upper D_e range and OD values of 45%, 47% and 44%, respectively. While none of the IR and pIR grains failed to intercept with the according DRC, about 2% of all measured grains suffered from this during fading correction and few grains plot above the 86% saturation limit (IR_{corr}: 6; pIR: 11). For this partially bleached, type A sample, corrected SG IR MAM D_e values of 346 ± 12 Gy and 352 ± 28 Gy were derived for the T_n threshold approach and the 30% of brightest grains, respectively. This converted to MAM apparent ages of 186 ± 9 ka and 210 ± 18 ka, respectively. While the MAM age obtained using the T_n threshold agrees with the finite age of the SG OSL signal, the use of only 30% off the brightest grains presents a slightly higher value.

For the SG pIR signal, a MAM D_e value of 271 ± 17 Gy and a MAM apparent age of 146 ± 11 ka were yielded. Interestingly, while the SG pIR MAM apparent age is somewhat lower than the finite SA age, both SG IR MAM age estimates are much higher than the finite age of the SA dataset.

5.2.3. Sample: RINI4-1

While SA D_e distributions of both RIN samples are similar in shape, those of the outcrop samples RINI4-1 appear to be much broader. The OSL D_e distribution of RINI4-1 is positively skewed, truncated and shows an OD value of 32%. However, most aliquots are well below $2*D_0$, suggesting that high dose responses beyond single exponential behaviour, as often observed for samples from the region (Lowick et al., 2010; Dehnert et al., 2012), is unaccountable for the spread in D_e values. An explanation for saturated aliquots and those that contribute to the skew may rather be partial bleaching. When applying the MAM, only two very low D_e values are considered for age determination, while the CAM appeared to best describe the lower part of the distribution that seems to be almost normally distributed. Using the MAM and the CAM, D_e values of 215 ± 23 Gy and 299 ± 16 Gy are obtained, respectively. Those correlate to OSL apparent ages of either 145 ± 18 ka or 202 ± 16 ka for this truncated distribution.

Similarly, most aliquots of the IR and pIR measurements ploted between 86% and 95% saturation and some failed to intersect with the respective SGC. D_e distributions of both IR and pIR signals present a much wider spread and a positive skew. These distributions give IR_{corr} and pIR D_e estimates of 702 ± 73 Gy and 671 ± 78 Gy using the MAM. Those results are statistically consistent with each other and may denote apparent age estimates of 304 ± 35 ka and 291 ± 37 ka, which lie well above the OSL MAM and CAM apparent age estimates.

For the SG OSL measurements of RINI4-1, only 6 out of the measured 6500 grains gave an acceptable D_e value. This is an insufficient number to investigate the SG D_e distribution and rather surprising as 36 out of 44 measured aliquots were accepted. Only few aliquots (3 SA; 7%) were rejected for a lacking fast component dominance, while the other 11% failed to intercept with the SGC (saturation; 5 SA). Less than 1% of the SG measurements were rejected as they were in saturation. Most SG measurements were excluded due to a dim signal (85%) or for unsuitable DRC fitting (FOM >10; 13%). In absence of a substantial SG OSL dataset, it is speculative what contributed to the SA signals and how reliable any obtained age from this approach is.

In comparison to the already broad SA D_e distributions of RINI4-1, the SG IR and pIR distributions spread even wider (OD 69%, 50%, respectively) and were more positively skewed. Only few grains were in saturation, while only twelve grains of the IR_{corr} signal plotted beyond 86% saturation. However, about half of the pIR measurements intercepted the respective DRC above 90% saturation. For this partially bleached type C sample, MAM D_e values of 211 ± 28 Gy and 496 ± 77 Gy as well as the associated MAM apparent age estimates of 92 ± 13 ka and 215 ± 35 ka were derived for the IR_{corr} and pIR signals, respectively. This might either indicate a failing of the fading correction for IR or that none or only insignificantly few grains had fully bleached pIR signals before deposition. However, SG fading correction has been shown to perform well for other samples of this dataset (e.g. RIN4, UST1) and the SG pIR distribution shows a much slower increase in the low part of the D_e distribution. This is a likely indicator for the lack of a fully bleached component in the pIR signal. Both SG MAM apparent age estimates are much lower than those derived using the SA OSL (202 ± 16 ka), IR (304 ± 35 ka) and pIR (291 ± 37 ka) approach, suggesting that the averaged signals of the latter mask a potentially well bleached proportion of grains. Hence, the SG IR_{corr} MAM age estimate of 92 ± 13 ka represents the most precautious attempt to date this sample.

5.2.4. Sample: HABS1-3

The SA OSL D_e distribution of HABS1-3 showed a positively skewed shape, with an OD value of 35%. For this sample, most aliquots were well below the $2*D_0$ value of the respective SGC. The MAM was applied yielding a D_e value of 131 ± 19 Gy and an apparent age of 67 ± 10 ka. While the uncorrected IR D_e distributions resembled that of the sample's respective OSL signal, the corrected D_e distribution wad widely spread and truncated due to aliquots in saturation (no interception with the SGC). The majority of aliquots showed D_e values above 90% or 95% saturation and are slightly higher than the pIR D_e values. While this could be related to the applied fading correction, it is a likely expression of the IR signal approaching saturation. The sample yielded a MAM D_e value of 856 ± 63 Gy and an apparent age of 337 ± 30 ka.

In contrast to the uncorrected IR D_e distributions, the pIR signals present wider distributions and a more positive skew suggesting, insufficient bleaching of the latter. In addition, the majority of measured aliquots intersected above 86% or 90% saturation with the respective SGC but all measured aliquots intersect with the SGC. A MAM D_e value of 805 ± 54 Gy was derived and accordingly, an apparent pIR age of 317 ± 26 ka could be suggested. The resemblance of the IR_{corr} and uncorrected pIR D_e distributions, especially at the low range, is noteworthy. This suggests either that those aliquots consisted of well or equally poorly bleached grains, which is reflected in the pIR and IR_{corr} apparent ages being statistically consistent with each other. Similar to RINI4-1, the IR and pIR apparent ages are much higher than the OSL age estimate.

Unfortunately, the limited amount of Q purified from HABS1-3 prevented SG measurements and thereby the direct comparison of these signals. For SG pIR and IR_{corr} measurements, the D_e distributions are widely spread (OD 45% and 57%, respectively), positively skewed with a tail towards the high D_e range and at least the IR_{corr} distribution is truncated due to 11% of grains being in saturation (no interception with the SGC). For a substantial number of grains (half of all accepted), the pIR measurements intercepted the respective DRC beyond 90% saturation, while this is true for only few grains of the IR_{corr} measurements. The sample yielded a SG IR_{corr} MAM D_e value of 254 ± 29 Gy and a MAM apparent age of 100 ± 12 ka. For the pIR signal, MAM D_e values of 763 ± 148 Gy and 717 ± 135 Gy were obtained for the T_n threshold cleaned dataset and for the 30% of brightest grains (type B). This corresponds to MAM apparent ages of 300 ± 60 ka and 282 ± 55 ka, respectively. Both pIR apparent age estimates are much higher than the IR_{corr} MAM age, but statistically consistent with both the IR_{corr} and pIR MAM apparent ages of the SA dataset. As this dataset is derived from an average signal, it is likely that partially bleached grains are contributing to the D_e values for D_e determination and thus may indicate that even the lower values of the pIR D_e distribution were not fully bleached before deposition. Therefore, an SG IR_{corr} MAM age of 100 ± 12 ka may describe this sample best.

5.3. Strassberg Trough

Similar to the older samples from the Lower Aare Valley, for both samples from the Strassberg Trough, OSL measurements were unfeasible.

5.3.1. Sample: HST2

For measurements of HST2, both SA IR signals were well below the 86% saturation limit and all aliquots intersected the SGC. D_e values of the IR signals (corrected and uncorrected) yielded an OD value of 15% and are narrowly distributed with only one or two outliers in the upper range. CAM and nMAD CAM D_e values are both 391 Gy implying that the outliers have little influence on the average. The shapes of the distributions are almost identical to those of GBR1. The pIR D_e distribution presents a positive skew with a rather low OD value of 20%. Both nMAD CAM and MAM give consistent pIR D_e values with 564 ± 19 Gy and 572 ± 43 Gy, respectively. The respective pIR apparent ages are 321 ± 18 ka and 325 ± 28 ka while IR_{corr} D_e values of HST2 yield a much lower nMAD CAM apparent age of 222 ± 11 ka.

All HST2 SG D_e distributions are widely spread, show a distinct tail towards the high range and present OD values over 49%; all characteristic for a partially bleached sample. For the IR_{corr} signal, 4% of grains show saturation, while only the pIR signal of one grain fails to intercept with its DRC. More than half of both the IR_{corr} and pIR signals plot beyond the 86% or even 90% saturation limits on the respective DRC. As a type A sample, the SG IR_{corr} dataset was cleaned leading to a notable change of shape in the lower part of the D_e distribution and a reduction

in OD values to 40% and 39% for the T_n threshold approach and the 30% of brightest grains, respectively. Those cleaned distributions yielded SG MAM D_e values of 359 ± 47 Gy and 379 ± 54 Gy, with corresponding MAM apparent ages of 204 ± 28 ka and 215 ± 13 ka. A MAM apparent age of 184 ± 25 ka for the SG pIR signal (323 ± 42 Gy) correlates well with both IR estimates. While all three apparent ages are expectably much lower than the SA pIR apparent age, they are in agreement with the SA IR_{corr} apparent age. However, the latter is an averaged value derived from a combination of grains that included those dimmer grains deemed unreliable for type A samples, as well as those identified as partially bleached on a SG level. The masking of such components in the SA signal is also expressed in the agreement between SA and SG CAM D_e values. Hence, a MAM age of 184 ± 25 ka to 215 ± 13 ka may describe the depositional age of this sample best.

5.3.2. Sample: HST15

While the uncorrected SA IR D_e distribution of HST15 mirrors that of HST2, the SA IR_{corr} and pIR D_e distributions presented a much wider spread, a more positive skew and are truncated due to aliquots in saturation. However, the majority of aliquots shows D_e values below 86%. Noteworthy is the resemblance of the IR_{corr} and uncorrected pIR D_e distributions, especially at the low range. This suggests that those aliquots consisted of either well or equally poorly bleached grains, which is reflected in the pIR and IR_{corr} apparent ages being statistically consistent with each other. The sample yielded MAM D_e values of 795 ± 73 Gy and 925 ± 61 Gy with apparent ages 415 ± 41 ka and 483 ± 37 ka for the IR_{corr} and uncorrected pIR signals, respectively.

In comparison to HST2, HST15 presented even wider SG D_e distributions, with OD values of 47% and 76% for the pIR and IR_{corr} signals. Both distributions were truncated with 8% and 11% of grains in saturation and consist of one third to two third of grains that plotted beyond the 90% saturation limit on the respective DRCs, respectively. As a type C sample, all D_e values were included to derive SG MAM D_e values of 149 ± 22 Gy (IR_{corr}) and 491 ± 71 Gy (pIR). These D_e values correspond to MAM apparent age estimates of 78 ± 12 ka and 256 ± 38 ka, respectively. A resemblance of IR_{corr} and uncorrected pIR D_e values in the low range, as found for SA, was lacking for the SG measurements. While this may indicate that the aliquots measured rather consisted of equally poorly bleached grains than well bleached ones which is reflected in the much higher SA apparent age estimates of 415 ± 41 ka (IR_{corr}) and 483 ± 37 ka (pIR), it is expected for HST15 to be older than an HST2 which was deposited 113 m above. The latter yielded MAM apparent age estimates of 184 ± 25 ka to 215 ± 13 ka, hence, a MAM age estimate for HST15 may be best represented by pIR with 256 ± 38 ka.

6. Discussion

6.1. The luminescence signal of quartz

Comparing SA and SG OSL results for RIN2 (SA: 190 ± 9 ka; SG: 206 ± 12 ka) and RIN4 (SA: 178 ± 9 ka; SG: 171 ± 8 ka), the ages agree within 1 σ uncertainty. The SG measurements of both samples yielded rather dim signals and the fast component was not dominant. While the fast component is considered to provide a thermally stable signal, some other components, i.e. the medium component, are thought to be thermally unstable and hence give lower D_e value (Li and Li, 2006). However, the SA measurements in this study presented bright signals and fast component dominance, likely suggesting that firstly, the summed signal of multiple grains in the SA measurements is representative of those individual grains that have passed SG rejection criteria and that secondly, the lack of a dominant detectable fast component in the SG measurements may indeed be related to the signal-to-background ratio, which prevents the mathematically derivation of such components.

For GBR1, the calculated SG apparent age exceeds that derived from the SA measurements by about 20 ka (SA: 64 ± 4 ka; SG: 86 ± 1 ka). As expected from the necessity of IR screening and fast component assessment of the SA measurements, many grains of this sample failed the applied SG rejection criteria and less than 1% were used for final D_e determination. However, those grains passing all rejection criteria presented bright natural signals, which is in contrast to the comparatively dim SA signal. This indicates that averaged SA signals might still be impacted by the contribution of grains without dominant fast components. Nevertheless, the application of an early background subtraction to maximise the fast component contribution of the used signal, as suggested by Cunningham and Wallinga (2010), would reduce the SA OSL D_e value from 82 ± 4 Gy to 71 ± 3 Gy (64 ± 4 ka to 55 ± 4 ka; nMAD CAM) and thereby increase the discrepancy between the SA and SG results. It appears that grains without dominant fast components may only contribute a small part, if any, to the averaged SA OSL signal and that other masked drivers are responsible for the lower D_e values. This is in accordance with findings by Trauerstein et al. (2017) who observed SA OSL signals dominated by the medium and slow components for samples from northern Switzerland, but the rejection of those SA measurements remained without impact onto the finite D_e values. Also, Bickel et al. (2015) found that the influence of a potentially thermally unstable component in their SA OSL signal for samples from the eastern Alps was negligible. In contrast, Klasen et al. (2016) decided to suspend the use of OSL measurements, as they observed thermal instability for SA measurements of deposits from the north-eastern Alpine foreland. Interestingly, for similar deposits from the wider Alpine region, thermal stability of the OSL signal was reported (Gaar et al., 2013; Salcher et al., 2015; Schielein et al., 2015). The presence and absence of thermal stability might well be linked to the intricate geological constitution of the Alps including magmatic and metamorphic origins. In addition to provenance, the bleaching and dose accumulation history of the Q grains might contribute to disparities in luminescence characteristic (Preusser et al., 2006).

Considering the luminescence characteristics and performance of individually measured Q grains and the internal consistency with results of SG F measurements, the SG Q age for GBR1 appears most reliable. Interestingly, for RINI4-1 both SA and SG OSL measurements yielded bright signals and appeared to be fast component dominated. A finite age comparison was prevented by the insufficient number of SG measurements passing the rejection criteria (6 out of 6500). The obtained SG D_e values plotted at the lower end of the SA D_e distribution or below (Fig. S7), which is in contrast to observations from GBR1. However, the SA dataset already indicated a partially bleached signature, which might mask the impact of grains with lower D_e values as seen for GBR1 and explain a trend towards higher SA D_e values. It was suggested that RINI4-1 was deposited in a rather distal position from the ice margin (Graf et al., 2006) but it appears that sunlight exposure during transport was still insufficient.

Considering the diverse nature of the samples presented here, it has been shown that SG measurements allow for a more thorough investigation of the luminescence signals and allow to select those grains with D_e values that most likely represent the depositional age. The dominance of a fast component is not necessarily an effective SA rejection criterion and not all samples presented in this study have a sufficient amount of Q with appropriate luminescence characteristics.

6.2. Drivers of feldspar D_e distribution shape

Most investigated samples presented SG D_e distributions with OD values that were far above the OD values observed in dose recovery tests (Tables S3 and S5). While the upper range of those D_e distributions is expected to be driven by partial bleaching of those water-transported samples, the spread towards the lower end of the D_e distributions needs further discussion. This was in turn pivotal for such samples, as the isolation of a population of grains that are indeed thought to represent the well bleached fraction is needed for the constraint of age estimates using the MAM. Dependencies between low D_e values and either recuperation, recycling or DRC fitting (FOM) were found for

neither the SG measurements of the IR nor the pIR signals.

Signal brightness as a driver has previously been observed in various studies (cf. Zhang and Li, 2020). For example, Reimann et al. (2012) attributed lower SG D_e values to lower potassium content in dimmer grains of marine deposits from north-eastern Germany. The 30% of brightest grains were found to give reliable pIR age estimates that agreed with independent age controls. Correspondingly, Smedley (2014) suggested the use of the 20% brightest grains for coastal dune samples from New Zealand for which a dependency between brightness, potassium content and D_e values was observed. However, this dependency was lacking for samples from proglacial deposits of Great Britain (Smedley et al., 2019).

Jacobs et al. (2019) found a similar relationship of signal brightness to the natural D_e value as to those determined during dose recovery tests (T_n threshold plateaus), unlike the observations of this study. They concluded that the individual potassium content of the grains has a smaller impact on the D_e distribution shapes. Guo et al. (2015) observed low D_e values in relation to low signal intensity, suggesting that sensitivity changes in dim grains occurred between the measurement of the natural signal and the following test dose. Other studies observed a relationship between brightness and fading rates of individual grains. For alluvial terrace samples from Mexico, Brown et al. (2015) determined that the brightest 25% of grains are likely to represent a non-fading population of the measured pIR signal, as those yielded ages in agreement with independent age control. Guo et al. (2020) also observed higher fading rates for dimmer grains from alluvial-diluvial deposits from northern China using a MET pIR protocol. For the IR signal, Trauerstein et al. (2012) also found higher g-values and scatter for dimmer grains of samples from the south-western Rub' al Khali in Saudi Arabia. However, individual pIR fading rates determined by Reimann et al. (2012) and Rhodes (2015; various deposits from around the world) appear to be less impacted by the brightness of the grains.

While most of the studies mentioned above apply a "cleaning" of the D_e distributions (T_n threshold plateau, % of brightest grains) prior to age estimation, many still report discrepancies between derived ages and independent age control or those derived using multi grain measurements (Reimann et al., 2012; Trauerstein et al., 2012; Smedley, 2014; Rhodes, 2015; Smedley et al., 2019). Possible explanations for the persistence of low SG D_e values are suggested by the contamination of samples during collection or preparation (Smedley, 2014), intrusive grains caused by, for example bioturbation (Rhodes, 2015), grain migration (Reimann et al., 2012), variability in SG internal Rb content or measurement accuracy (Buylaert et al., 2019), inapplicability of the used fading correction (Trauerstein et al., 2012) and microdosimetry (Reimann et al., 2012; Smedley et al., 2019). In general, consensus of multiple drivers for the occurrence of unexplainably low SG F D_e values is reached.

None of the samples investigated in this study presented a dependency between individual grain brightness and dose recovery test results (Fig. 9 and S6), suggesting that sensitivity change is equal in dim and bright grains, and hence, can be excluded as a possible cause for the occurrence of low D_e values. Individual IR fading rates presented a wider scatter for dim grains than for bright grains while no such relationship was observed for the pIR signal (Fig. 10). However, a dependency between signal brightness and natural D_e value was observed (Fig. 9 and S6) for either the IR or pIR signal of some samples (type A and B) or not at all (type C). The individual fading rates directly impacted the natural D_e distributions (IR) of type A samples, however, it is possible that fading of the IR D_e values of type B and C samples are masked by competing drivers. In the absence of potassium content measurements for the samples presented in this study, a direct comparison remains lacking. However, the most conservative approach for samples with various potassium contents (30% brightest grains) was compared to the warranted cleaning of D_e distributions of type A and B samples, which was applied following the T_n threshold plateau approach. It was shown that a brightness cleaning step in the absence of a T_n threshold plateau is inappropriate, suggesting, either that variations in potassium content of the investigated samples were negligible or that their effects were sufficiently masked by other drivers contributing to the derived D_e values. Similar to other studies, even after the application of a brightness cleaning step, low D_e values persisted in the distributions. The systematic appearance of this phenomenon in the presented dataset, as well as the literature, makes it unlikely to find possible causes in the contamination of samples during collection or preparation, intrusive grains from bioturbation, grain migration, measurement accuracy or the inapplicability of the used fading correction. However, the variability in SG internal Rb content and microdosimetry are potential sources for scatter in SG D_e distributions. On the basis of this dataset, a differentiation of the sources is unfeasible and further investigations are needed.

While for well bleached samples, the phenomenon of low D_e values is less problematic as those values seem to have a negligible impact on the results of mean age models, for partially bleached deposits, of which the lower part of the population is targeted to derive a depositional age estimate, no such compensation occurs. Hence, deriving IR_{corr} and pIR MAM D_e values from distributions, cleaned or uncleaned, as presented in this study, will lead to the incorporation of such low D_e values as described above. However, it allows the constraint of the lowest depositional ages that are likely to underestimate the true burial time. The results of this rather conservative approach will hence be called "absolute minimum age estimates" and denoted with a ">"-sign (Fig. 2). In conclusion, these results show that for samples from northern Switzerland it is recommendable to compare luminescence signals obtained from both Q and F dosimeters to assess partial bleaching, as suggested by Trauerstein et al. (2017). Additionally, while it has been shown that the measurement of individual grains comes with some shortcomings, it also allows for the inspection of many aspects of the luminescence signals that even small aliquots would mask.

6.3. Constraining depositional age

For only two samples (GBR1, RIN2) agreeing SA OSL, IR_{corr} and pIR apparent ages could be derived (Fig. 2). For GBR1, SG measurements of the same signals also provided consistent estimates (Fig. 2). However, the finite SG ages of 86 ± 1 ka (OSL) and 89 ± 10 ka (IR_{corr}) and the pIR absolute minimum age of >73 ± 9 ka are somewhat higher than those of the SA measurements (61 ± 3 ka to 64 ± 4 ka). With the advantages of excluding many unfavourable grains and the internal consistency of ages, the SG dataset is considered more reliable for constraining a finite depositional age estimate. The other sample yielding consistent SA age estimates (RIN2) also showed an apparent SG OSL age in agreement. For the SG pIR and IR_{corr} datasets, only absolute minimum age estimates could be derived, which are lower than the OSL ages. This is not contradictory as the absolute minimum ages will underestimate the true burial age. Hence, a finite depositional age of between 176 ± 8 ka (SA IR_{corr}) and 206 ± 12 ka (SG OSL) can be expected.

One sample (RIN4) presented consistency between SA OSL (186 ± 10 ka) and pIR (176 ± 9 ka) apparent ages, while the SA IR_{corr} age (119 ± 5 ka) was significantly lower. Noteworthy is the low g-value determined for RIN4 (1.0 ± 0.7) that might have led to an underestimation of the SA apparent IR_{corr} age if the g-value estimate is incorrect. SG apparent age estimates of Q and of the brightness cleaned SG IR_{corr} dataset (T_n threshold) are in agreement and supported by the SG pIR absolute minimum estimate (>156 ± 11). However, analysing the F luminescence properties on a SG basis showed that SA results may mask effects of mutually compensating unfavourable luminescence characteristics. Therefore, a depositional age of this sample may be constrained from both Q ages of 171 ± 8 ka (SG) and 178 ± 9 ka (SA), and the SG IR_{corr} absolute minimum estimate of >186 ± 9 ka.

For those samples without SA OSL control, either SA ages in agreement (HST15, UST1) or higher pIR minimum ages in comparison to the IR_{corr} apparent ages (GBR12, HST2, UST3) are obtained.

For the two samples (HST15, UST1) with SA apparent ages in

agreement, however, ages derived using SG measurements were significantly lower. For UST1, it was shown that the SG brightness cleaning is redundant for both signals and that the SA dataset (IR_{corr}: 79 ± 5; pIR: 79 ± 10) may mask a partially bleached component. Thus, minimum SG age estimates of >56 ± 5 ka (IR_{corr}) and >48 ± 9 ka (pIR) are suggested to best describe the depositional age. Similarly, for HST15, masking of a partially bleached component in the SA dataset (IR_{corr}: 426 ± 25; pIR: 474 ± 24) is likely to be present (see section 5) and it is suspected that even the lowest population of SG pIR D_e values suffered from partial bleaching. However, from the stratigraphic position HST15 must have been deposited prior to HST2 and would hence be older. Therefore, the SG pIR minimum age of >256 ± 38 ka may be best to constrain the depositional age of this sample.

Other samples without OSL control yielded higher SA pIR apparent ages in comparison to the SA IR_{corr} ages (GBR12, HST2, UST3), even with the MAM pIR approach (see section 5). The SG datasets for GBR12 and UST3 suggested strong evidence for partial bleaching, with only the lowest population of the IR_{corr} D_e values having the potential to have been fully bleached prior to deposition. However, those D_e distributions also contained low D_e values from an unexplainable origin (see section 6.2). Hence, absolute minimum age estimates for those samples are constrained from the SG IR_{corr} signals to >92 ± 22 ka (GBR12) and >104 ± 14 ka (UST3). Similarly, the SG measurements of HST2 show a partially bleached distribution, but agreement between SG pIR and IR_{corr} (brightness cleaned) MAM apparent ages. This allows for constraining an absolute minimum depositional age between >148 ± 25 ka and >204 ± 18 ka using the SG dataset. As both estimates underestimate the true burial age, the higher IR_{corr} absolute minimum depositional age might be more precise. While SA IR_{corr} apparent ages are consistent with these age constraints, they are likely the result of masking by mutually compensating unfavourable luminescence characteristics (i.e. unexplainably low D_e values, differential bleaching).

For two samples (HABS1-3, RINI4-1), agreement between SA IR_{corr} and pIR apparent ages were observed while the SA OSL age was much lower. Both samples showed a majority of SA OSL D_e values equivalent to ages below the suspected upper limit of Q dating at 200 ka (Lowick et al., 2015). However, both SA OSL D_e distributions presented a positively skewed scatter that seemed to have a wider shape than the close-to normally distributed SA IR D_e values, at least for HABS1-3. The same grain size was used for both minerals, providing that all grains would have been subject to the same conditions regarding sunlight exposure and bleaching rates during transport, microdosimetry heterogeneity, post depositional mixing and sample contamination. While there is no evidence for the latter two to have occurred, differences in microdosimetry would be expected to cause a larger scatter in SA OSL D_e values, as the internal dose rate is much lower and hence the beta dose impact relatively larger (e.g. Jacobs, 2008). In addition, another cause of scatter could be found in the differential bleaching of the minerals. It is well established that Q bleaches much faster than both IR and pIR signals (e.g. Colarossi et al., 2015) and that only very few Q grains (<1%) of the region emit OSL signals as reported for sample RIN2 by Mueller et al. (2020). For the same sample, they found that 16% of F grains inherited an effective bright natural luminescence signal. While more grains of Q (ca. 50 to 200 grains) than of F (ca. 10 grains) were measured together on SA, it may well be that either or both signals consisted of the contribution of multiple grains and therefore represent an averaged value. Averaged D_e values may mask the impact of partial bleaching, and hence, prevent its assessment using SA measurements (e.g. Duller, 2006).

For HABS1-3 and RINI4-1, a direct comparison between SA and SG OSL was prohibited by lack of material (HABS1-3) or efficient luminescence signals (RINI4-1). However, the latter raises the question about what contributed to SA OSL measurements. The SG F datasets of both samples confirmed the observation of partial bleaching from the SA datasets and indicated that even the lower population of the pIR signals was not fully bleached before deposition. Hence, for both samples SG IR_{corr} absolute minimum age estimates are considered representative of deposition and yielded ages of >92 ± 13 ka (RINI4-1) and >100 ± 12 ka (HABS1-3).

Interestingly, all samples presented a partially bleached component in the IR and pIR signals. This occurs regardless of whether they were, based on the sedimentary facies, attributed to a setting that is rather proximal (GBR1, HST2, UST2) or distal (GBR12, HABS1-3, RIN2, RIN4, RINI4-1, HST15, UST3) to the respective expected ice margin. This indicates that conditions during transport hampered adequate exposure to sunlight to fully bleach those F signals. However, sunlight exposure appears to have been sufficient for Q with its faster bleaching abilities, as both the inferred proximal (GBR1) and distal (RIN2, RIN4) samples were well bleached. This is in contrast to findings of Alexanderson and Murray (2012), who observed full bleaching of the Q and IR signals for modern Arctic samples already in proximity to the ice margin with transport distances of ca. 500 m.

7. Conclusions

The investigated samples represent a broad range of glacially sourced deposits from northern Switzerland. While there is no obvious connection between bleaching and distal or proximal deposition in relation to the proposed ice margin, SG F measurements of most samples seem to reveal a partially bleached signature. This appears to be masked in the respective SA measurements (IR and pIR), even though only few grains emit luminescence signals during IR stimulation and small aliquots (ca. 10 grains) were used to reduce the averaging effect. Such masking is expressed in close-to-normal shaped D_e distributions and rather low OD values. Agreement between fading corrected IR and pIR D_e values might also lead to the assumption that SA measurements record the well bleached signature of the sample's D_e distribution, as both signals have distinctly different bleaching rates. However, it appears that the utilisation of the SA F measurements may well lead to overestimation of depositional age estimates. In addition, this approach obscures the occurrence of low D_e values that contribute to an average signal. While the drivers that cause these low D_e values cannot be isolated completely, the number of such values can be reduced in the presence of a T_n threshold plateau. The application of the pIR protocol on a SG level allows the various contributions to the different F signals (IR, pIR) to be untangled and gives valuable insights into the bleaching degree of glacially sourced deposits of northern Switzerland. Consequently, an approach to constrain the absolute minimum depositional age estimate of samples with D_e distributions containing both partially bleached grains and grains with unexplainably low D_e values can be found in the application of the MAM for SG measurements. It is to be mentioned that this absolute minimum depositional age is rather conservative and will likely underestimate the true depositional age.

In addition, SG measurements appear to be advantageous for Q as well. While the dominance of a fast component is not necessarily an effective SA rejection criterion for samples of this study, Q SG measurements allow the selection of those grains with D_e values that most likely represent the depositional age. However, not all samples presented in this study had a sufficient amount of Q with appropriate luminescence characteristics. However, from the results of this study, it is recommended to conduct both IR and pIR investigations in combination with Q measurements on a SG level.

The dating potential of the investigated deposits remains rather limited, yet, in this sedimentologic context the results presented revealed that glacial advances occurred during MIS 6 or earlier.

CRediT authorship contribution statement

Daniela Mueller: Writing – review & editing, Writing – original draft, Visualization, Methodology, Investigation, Funding acquisition, Formal analysis, Data curation, Conceptualization. **Lukas Gegg:** Writing – review & editing, Writing – original draft. **Alexander Fülling:** Data

curation. **Marius W. Buechi:** Writing – review & editing, Writing – original draft. **Gaudenz Deplazes:** Writing – review & editing, Funding acquisition. **Frank Preusser:** Writing – review & editing, Methodology, Conceptualization.

Declaration of competing interest

The authors declare the following financial interests/personal relationships which may be considered as potential competing interests: Daniela Mueller reports financial support was provided by National Co-operative for the Disposal of Radioactive Waste. Lukas Gegg reports financial support was provided by National Co-operative for the Disposal of Radioactive Waste. Alexander Fuelling reports financial support was provided by National Co-operative for the Disposal of Radioactive Waste. Marius Buechi reports financial support was provided by National Co-operative for the Disposal of Radioactive Waste. Gaudenz Deplazes reports financial support was provided by National Co-operative for the Disposal of Radioactive Waste. If there are other authors, they declare that they have no known competing financial interests or personal relationships that could have appeared to influence the work reported in this paper.

Data availability

Data will be made available on request.

Acknowledgement

This research has been supported by the National Cooperative for the Disposal of Radioactive Waste (NAGRA), Switzerland ("ZFT Nr. ZVK 2017 07 14 03" and "ZFT Nr. ZVK 2019 08 09"). The Lexsyg Research reader used in this study was financed through the Major Research Instrumentation Programme of the German Research Foundation (DFG), granted to FP (INST 39/996–1, project number 282256512). Support on the drill sites by Luka Seslak, as well as by Andrea Kuster, Dominik Amschwand, Marius Huber, and Kim Lemke during core processing was highly appreciated. The authors would like to thank Lisa Ahlers and Melanie Schulz for their support in the Freiburg OSL laboratory and Flavio Anselmetti for permission and support during the usage of the Bern OSL laboratory. We are grateful to William McCreary for proof reading. This manuscript was greatly improved through the comments of two anonymous reviewers.

Appendix A. Supplementary data

Supplementary data to this article can be found online at https://doi.org/10.1016/j.quageo.2024.101551.

References

Ali, S.N., Singh, P., Arora, P., Bisht, P., Morthekai, P., 2022. Luminescence dating of late pleistocene glacial and glacio-fluvial sediments in the Central Himalaya, India. Quat. Sci. Rev. 284, 107464 https://doi.org/10.1016/j.quascirev.2022.107464.

Alexanderson, H., Murray, A.S., 2012. Luminescence signals from modern sediments in a glaciated bay, NW Svalbard. Quat. Geochronol. 10, 250–256. https://doi.org/10.1016/j.quageo.2012.01.001.

Amschwand, D., Huber, M.L., Madritsch, H., Deplazes, G., Buechi, M.W., 2020. Quaternary Boreholes QBO Hochfelden-Strassberg (QHST), p. 12. Data Report. Nagra Arbeitsbericht NAB 20-02.

Anselmetti, F.S., Drescher-Schneider, R., Furrer, H., Graf, H.R., Lowick, S.E., Preusser, F., Riedi, M.A., 2010. A ~180,000 years sedimentation history of a perialpine overdeepened glacial trough (Wehntal, N-Switzerland). Swiss J. Geosci. 103, 345–361. https://doi.org/10.1007/s00015-010-0041-1.

Anselmetti, F.S., Bavec, M., Crouzet, C., Fiebig, M., Gabriel, G., Preusser, F., Ravazzi, C., DOVE scientific team, 2022. Drilling Overdeepened Alpine Valleys (ICDP-DOVE): quantifying the age, extent, and environmental impact of Alpine glaciations). Sci. Drill. 31, 51–70. https://doi.org/10.5194/sd-31-51-2022.

Arnold, L.J., Bailey, R.M., Tucker, G.E., 2007. Statistical treatment of fluvial dose distributions from southern Colorado arroyo deposits. Quat. Geochronol. 2, 162–167. https://doi.org/10.1016/j.quageo.2006.05.003.

Auclair, M., Lamothe, M., Huot, S., 2003. Measurement of anomalous fading for feldspar IRSL using SAR. Radiat. Meas. 37, 487–492. https://doi.org/10.1016/s1350-4487(03)00018-0.

Bailey, R.M., 2000. The interpretation of quartz optically stimulated luminescence equivalent dose versus time plots. Radiat. Meas. 32, 129–140. https://doi.org/10.1016/s1350-4487(99)00256-5.

Berger, J.-P., Reichenbacher, B., Becker, D., Grimm, M., Grimm, K., Picot, L., Storni, A., Pirkenseer, C., Schaefer, A., 2005. Eocene-pliocene time scale and stratigraphy of the upper rhine graben (URG) and the Swiss Molasse Basin (SMB). Int. J. Earth Sci. 94, 711–731. https://doi.org/10.1007/s00531-005-0479-y.

Bickel, L., Lüthgens, C., Lomax, J., Fiebig, M., 2015. Luminescence dating of glaciofluvial deposits linked to the penultimate glaciation in the Eastern Alps. Quat. Int. 357, 110–124. https://doi.org/10.1016/j.quaint.2014.10.013.

Bluszcz, A., Adamiec, G., 2006. Application of differential evolution to fitting OSL decay curves. Radiat. Meas. 41, 886–891. https://doi.org/10.1016/j.radmeas.2006.05.016.

Breuer, S., Bebiolka, A., Lang, J., 2023. The past is the key to the future - considering Pleistocene subglacial erosion for the minimum depth of a radioactive waste repository. E&G J. Quat. Sci. 72, 113–125. https://doi.org/10.5194/egqsj-72-113-2023.

Brown, N.D., Rhodes, E.J., Antinao, J.L., McDonald, E.V., 2015. Single-grain post-IR IRSL signals of K-feldspars from alluvial fan deposits in Baja California Sur, Mexico. Quat. Int. 362, 132–138. https://doi.org/10.1016/j.quaint.2014.10.024.

Buechi, M.W., Lowick, S.E., Anselmetti, F.S., 2017. Luminescence dating of glaciolacustrine silt in overdeepened basin fills beyond the last interglacial. Quat. Geochronol. 37, 55–67. https://doi.org/10.1016/j.quageo.2016.09.009.

Buechi, M.W., Graf, H.R., Haldimann, P., Lowick, S.E., Anselmetti, F.S., 2018. Multiple Quaternary erosion and infill cycles in overdeepened basins of the northern Alpine foreland. Swiss J. Geosci. 111, 133–167. https://doi.org/10.1007/s00015-017-0289-9.

Buylaert, J.-P., Thiel, C., Murray, A.S., Vandenberghe, D.A., Yi, S., Lu, H., 2011. IRSL and post-IR residual dose recorded in modern dust samples from the Chinese Loess Plateau. Geochronometria 38, 432–440. https://doi.org/10.2478/s13386-011-0047-0.

Buylaert, J.-P., Jain, M., Murray, A.S., Thomsen, K.J., Thiel, C., Sohbati, R., 2012. A robust feldspar luminescence dating method for Middle and Late Pleistocene sediments. Boreas 41, 435–451. https://doi.org/10.1111/j.1502-3885.2012.00248.x.

Buylaert, J.-P., Újvári, G., Murray, A.S., Smedley, R.K., Kook, M., 2019. On the relationship between K concentration, grain size and dose in feldspar. Radiat. Meas. 120, 181–187. https://doi.org/10.1016/j.radmeas.2018.06.003.

Cohen, D., Jouvet, G., Zwinger, T., Landgraf, A., Fischer, U.H., 2023. Subglacial hydrology from high-resolution ice-flow simulations of the Rhine Glacier during the Last Glacial Maximum: a proxy for glacial erosion. E&G J. Quat. Sci. 72, 189–201. https://doi.org/10.5194/egqsj-72-189-2023.

Colarossi, D., Guller, G.A., Roberts, H.M., Tooth, S., Lyons, R., 2015. Comparison of paired quartz OSL and feldspar post-IR IRSL dose distributions in poorly bleached fluvial sediments from South Africa. Quat. Geochronol. 30, 233–238. https://doi.org/10.1016/jj.quageo.2015.02.015.

Cunningham, A.C., Wallinga, J., 2010. Selection of integration time intervals for quartz OSL decay curves. Quat. Geochronol. 5, 657–666. https://doi.org/10.1016/j.quageo.2010.08.004.

Degering, D., Degering, A., 2020. Change is the only constant - time-dependent dose rates in luminescence dating. Quat. Geochronol. 58, 1–14. https://doi.org/10.1016/j.quageo.2020.101074.

Dehnert, A., Lowick, S.E., Preusser, F., Anselmetti, F.S., Drescher-Schneider, R., Graf, H. R., Heller, F., Horstmeyer, H., Kemna, H.A., Nowactzyk, N.R., Züger, A., Furrer, H., 2012. Evolution of an overdeepened trough in the northern alpine foreland at niederweningen, Switzerland. Quat. Sci. Rev. 34, 127–145. https://doi.org/10.1016/j.quascirev.2011.12.015.

Duller, G.A., 1994. A new method for the analysis of infrared stimulated luminescence data from potassium feldspar. Radiat. Meas. 23, 281–285. https://doi.org/10.1016/1350-4487(94)90053-1.

Duller, G.A., 1997. Behavioural studies of stimulated luminescence from feldspars. Radiat. Meas. 27, 663–694. https://doi.org/10.1016/s1350-4487(97)00216-3.

Duller, G.A., 2003. Distinguishing quartz and feldspar in single grain luminescence measurements. Radiat. Meas. 37, 161–165. https://doi.org/10.1016/S1350-4487(02)00170-1.

Duller, G.A., 2006. Single grain optical dating of glacigenic deposits. Quat. Geochronol. 1, 296–304. https://doi.org/10.1016/j.quageo.2006.05.018.

Fu, X., Li, B., Jacobs, Z., Jankowski, N.R., Cohen, T.J., Roberts, R.G., 2020. Establishing standardised growth curves (SGCs) for OSL signals from individual grains of quartz: a continental-scale case study. Quat. Geochronol. 60, 101107 https://doi.org/10.1016/j.quageo.2020.101107.

Gaar, D., Preusser, F., 2012. Luminescence dating of mammoth remains from northern Switzerland. Quat. Geochronol. 10, 257–263. https://doi.org/10.1016/j.quageo.2012.02.007.

Gaar, D., Graf, H.R., Preusser, F., 2019. New chronological constraints on the timing of Late Pleistocene glacier advances in northern Switzerland. E&G J. Quat. Sci. 68, 53–73. https://doi.org/10.5194/egqsj-68-53-2023.

Gaar, D., Lowick, S.E., Preusser, F., 2013. Performance of different luminescence approaches for the dating of known-age glaciofluvial deposits from northern Switzerland. Geochronometria 41, 65–80. https://doi.org/10.2478/s13386-013-0139-0.

Galbraith, R.F., Roberts, R.G., Laslett, G.M., Yoshida, H., Olley, J.M., 1999. Optical dating of single and multiple grains of quartz from Jinmium rock shelter, Northern

Australia: Part I, experimental design and statistical models. Archaeometry 41, 339–364. https://doi.org/10.1111/j.1475-4754.1999.tb00987.x.
Gegg, L., Kuster, A.M., Schmid, D., Buechi, M.W., 2018. Quaternary Boreholes QBO Riniken-1 & -2 (QRIN1 & QRIN2). Data Report, vols. 18–40. Nagra Arbeitsbericht NAB, p. 8. https://www.nagra.ch/de/cat/publikationen/arbeitsberichte-nabs/nabs-2018/downloadcenter.htm.
Gegg, L., Kuster, A.M., Schmid, D., Lemke, K., Deplazes, G., Madritsch, H., Buechi, M.W., 2019a. Quaternary Boreholes QBO Untersiggenthal (QUST), p. 8. Data Report. Nagra Arbeitsbericht NAB 19-01. https://www.nagra.ch/en/cat/publikationen/arbeitsberichte-nabs/nabs-2019/downloadcentre.htm.
Gegg, L., Kuster, A.M., Deplazes, G., Madritsch, H., Buechi, M.W., 2019b. Quaternary Boreholes QBO Gebenstorf-Brüel (QGBR), p. 8. Data Report. Nagra Arbeitsbericht NAB 19-02. https://www.nagra.ch/en/cat/publikationen/arbeitsberichte-nabs/nabs-2019/downloadcentre.htm.
Gegg, L., Deplazes, G., Keller, L., Madritsch, H., Spillmann, T., Anselmetti, F.S., Buechi, M.W., 2021. 3D morphology of a glacially overdeepened trough controlled by underlying bedrock geology. Geomorphology 394, 107950. https://doi.org/10.1016/j.geomorph.2021.107950.
Gegg, L., Anselmetti, F.S., Deplazes, G., Knipping, M., Madritsch, H., Mueller, D., Preusser, F., Vogel, H., Buechi, M.W., 2023. Rinikerfeld Palaeolake (Northern Switzerland) - a sedimentary archive of landscape and climate change during the penultimate glacial cycle. J. Quat. Sci. 38, 174–185. https://doi.org/10.1002/jqs.3471.
Gegg, L., Preusser, F., 2023. Comparison of overdeepened structures in formerly glaciated areas of the northern Alpine foreland and northern central Europe. E&G J. Quat. Sci. 72, 23–36. https://doi.org/10.5194/egqsj-72-23-2023.
Godfrey-Smith, D.I., Huntley, D.J., Chen, W.H., 1988. Optical dating studies of quartz and feldspar sediment extracts. Quat. Sci. Rev. 7, 373–380. https://doi.org/10.1016/0277-3791(88)90032-7.
Graf, H.R., Bitterli-Dreher, P., Burger, H., Bitterli, T., Diebold, P., Naef, H., 2006. Geologischer Atlas der Schweiz 1:25.000, Blatt 1070 Baden. Bundesamt für Landestopografie, Swisstopo, Wabern.
Graf, H.R., 2009a. Stratigraphie von Mittel-und Spätpleistozän in der Nordschweiz. Beiträge zur Geologischen Karte der Schweiz. Swisstopo 168, 198.
Graf, H.R., 2009b. Stratigraphie und Morphogenese von frühpleistozänen Ablagerungen zwischen Bodensee und Klettgau. E&G J. Quat. Sci. 58, 12–53. https://doi.org/10.3285/eg.58.1.02.
Graf, H.R., Burkhalter, R., 2016. Quaternary deposits: concept for a stratigraphic classification and nomenclature - an example from northern Switzerland. Swiss J. Geosci. 109, 137–147. https://doi.org/10.1007/s00015-016-0222-7.
Gribenski, N., Valla, P.G., Preusser, F., Roattino, T., Crouzet, C., Buoncristiani, J.F., 2021. Out-of-phase Late Pleistocene glacial maxima in the Western Alps reflect past changes in North Atlantic atmospheric circulation. Geology 49, 1096–1101. https://doi.org/10.1130/g48688.1.
Guo, Y., Li, B., Zhang, J.F., Roberts, R.G., 2015. Luminescence-based chronologies for Palaeolithic sites in the Nihewan Basin, northern China: first tests using newly developed optical dating procedures for potassium feldspar grains. J. Archaeol. Sci. Rep 3, 31–40. https://doi.org/10.1016/j.jasrep.2015.05.017.
Guo, Y., Li, B., Zhao, H., 2020. Comparison of single-aliquot and single-grain MET-pIRIR De results for potassium feldspar samples from the Nihewan Basin, northern China. Quat. Geochronol. 56, 101040 https://doi.org/10.1016/j.quageo.2019.101040.
Hu, Y., Marwick, B., Zhang, J.F., Rui, X., Hou, Y.M., Yue, J.P., Chen, W.R., Huang, W.W., Li, B., 2019. Late Middle Pleistocene levallois stone-tool technology in southwest China. Nature 563, 82–85. https://doi.org/10.1038/s41586-018-0710-1.
Haldimann, P., Graf, H.R., Jost, J., 2017. Geologischer Atlas der Schweiz. 1071 Bülach (Atlasblatt 151). Erläuterungen, Bundesamt für Landestopografie, Swisstopo, Wabern.
Hu, Y., Li, B., Jacobs, Z., 2020. Single-grain quartz OSL characteristics: testing for correlations within and between sites in Asia, Europe and Africa. Methods Protoc 3 (2), 1–15. https://doi.org/10.3390/mps3010002.
Huntley, D.J., 2006. An explanation of the power-law decay of luminescence. J. Phys.-Condens. Mat. 18, 1359–1365. https://doi.org/10.1088/0953-8984/18/4/020.
Huntley, D.J., Baril, M.R., 1997. The K content of the K-feldspars being measured in optical dating or in thermoluminescence dating. Anc. TL 15, 11–13.
Huntley, D.J., Lamothe, M., 2001. Ubiquity of anomalous fading in K-feldspars and measurement and correction for it in optical dating. Can. J. Earth Sci. 38, 1093–1106. https://doi.org/10.1139/e01-013.
Jacobs, Z., 2008. Luminescence chronologies for coastal and marine sediments. Boreas 37, 508–535. https://doi.org/10.1111/j.1502-3885.2008.00054.x.
Jacobs, Z., Li, B., Shunkov, M.V. Kozlikin, Bolikhovskaya, N.S., Agadjanian, A.K., Uliyanov, V.A., Vasiliev, S.K., O'Gorman, K., Derevianko, A.P., Roberts, R.G., 2019. Timing of archaic hominin occupation of Denisova Cave in southern Siberia. Nature 565, 594–599. https://doi.org/10.1038/s41586-018-0843-2.
Jordan, P., Wetzel, A., Reisdorf, A., 2008. Swiss Jura Mountains. In: McCann, T. (Ed.), The Geology of Central Europe, vol. 2. Geological Society of London, London, pp. 823–923.
Kamleitner, S., Ivy-Ochs, S., Monegato, G., Gianotti, F., Akçar, N., Vockenhuber, C., Christl, M., Synal, H.A., 2022. The ticino-toceglacier system (Swiss-Italian Alps) in the framework of the alpine last glacial maximum. Quat. Sci. Rev. 279, 107400 https://doi.org/10.1016/j.quascirev.2022.107400.
Kars, R.H., Wallinga, J., Cohen, K.M., 2008. A new approach towards anomalous fading correction for feldspar IRSL dating—tests on samples in field saturation. Radiat. Meas. 43, 786–790. https://doi.org/10.1016/j.radmeas.2008.01.021.
King, G.E., Burow, C., 2019. Calc_Huntley2006: apply the Huntley (2006) model. Function version 0.4.1. In: Kreutzer, S., Burow, C., Dietz, M., Fuchs, M.C., Schmidt, C., Fischer, M., Friedrich, J. (Eds.), Luminescence: Comprehensive Luminescence Dating Data Analysis. R package version 0.9.0.109. https://CRAN.R-project.org/package=Luminescence.
Klasen, N., Fiebig, M., Preusser, F., 2016. Applying luminescence methodology to key sites of Alpine glaciations in Southern Germany. Quat. Int. 420, 249–258. https://doi.org/10.1016/j.quaint.2015.11.023.
Kock, S., Kramers, J.D., Preusser, F., Wetzel, A., 2009. Dating of Late Pleistocene terrace deposits of the River Rhine using Uranium series and luminescence methods: potential and limitations. Quat. Geochronol. 4, 363–373. https://doi.org/10.1016/j.quageo.2009.04.002.
Lai, Z.P., 2010. Chronology and the upper dating limit for loess samples from Luochuan section in the Chinese Loess Plateau using quartz OSL SAR protocol. J. Asian Earth Sci. 37, 176–185. https://doi.org/10.1016/j.jseaes.2009.08.003.
Lamothe, M., Auclair, M., Hamzaoui, C., Huot, S., 2003. Towards a prediction of long-term anomalous fading of feldspar IRSL. Radiat. Meas. 37, 493–498. https://doi.org/10.1016/s1350-4487(03)00016-7.
Li, B., Li, S.-H., 2006. Comparison of D_e estimates using the fast component and the medium component of quartz OSL. Radiat. Meas. 41, 125–136. https://doi.org/10.1016/j.radmeas.2005.06.037.
Li, B., Roberts, R.G., Jacobs, Z., Li, S.-H., 2015a. Potential of establishing a 'global standardised growth curve' (gSGC) for optical dating of quartz from sediments. Quat. Geochronol. 27, 94–104. https://doi.org/10.1016/j.quageo.2015.02.011.
Li, B., Roberts, R.G., Jacobs, Z., Li, S.-H., Guo, Y.J., 2015b. Construction of a 'global standardised growth curve' (gSGC) for infrared stimulated luminescence dating of K-feldspar. Quat. Geochronol. 27, 119–130. https://doi.org/10.1016/j.quageo.2015.02.010.
Li, B., Jacobs, Z., Roberts, R.G., 2016. Investigation of the applicability of standardised growth curves for OSL dating of quartz from Haua Fteah cave, Libya. Quat. Geochronol. 35, 1–15. https://doi.org/10.1016/j.quageo.2016.05.001.
Lowick, S.E., Preusser, F., Wintle, A.G., 2010. Investigating the linear region of quartz optically stimulated luminescence dose response curves at high doses. Radiat. Meas. 45, 975–984. https://doi:10.1016/j.radmeas.2010.07.010.
Lowick, S.E., Trauerstein, M., Preusser, F., 2012. Testing the application of post IR-IRSL dating to fine grain waterlain sediments. Quat. Geochronol. 8, 33–40. https://doi.org/10.1016/j.quageo.2011.12.003.
Lowick, S.E., Buechi, M.W., Gaar, D., Graf, H.R., Preusser, F., 2015. Luminescence dating of Middle Pleistocene proglacial deposits from northern Switzerland: methodological aspects and stratigraphical conclusions. Boreas 44, 459–482. https://doi.org/10.1111/bor.12114.
Mueller, D., Preusser, F., Buechi, M.W., Gegg, L., Deplazes, G., 2020. Luminescence properties and dating of glacial to periglacial sediments from northern Switzerland. Geochronol 2, 305–323. https://doi.org/10.5194/gchron-2-305-2020.
Mueller, D., Preusser, F., 2022. Investigating the applicability of a standardised growth curve approach on Middle Pleistocene sediments from northern Switzerland. Quat. Geochronol. 67, 101238 https://doi.org/10.1016/j.quageo.2021.101238.
Müller, P., Hoyer, E.-M., Bartetzko, A., Rühaak, W., 2023. Expected and deviating evolutions in representative preliminary safety assessments – a focus on glacial tunnel valleys. E&G J. Quat. Sci. 72, 73–76. https://doi.org/10.5194/egqsj-72-73-2023.
Murray, A.S., Wintle, A.G., 1999. Isothermal decay of optically stimulated luminescence in quartz. Radiat. Meas. 30, 119–125. https://doi.org/10.1016/s1350-4487(98)00097-3.
Murray, A.S., Wintle, A.G., 2000. Luminescence dating of quartz using an improved single-aliquot regenerative-dose protocol. Radiat. Meas. 32, 57–73. https://doi.org/10.1016/s1350-4487(99)00253-x.
Murray, A.S., Buylaert, J.-P., Henriksen, M., Svendsen, J.I., Mangerud, J., 2008. Testing the reliability of quartz OSL ages beyond the Eemian. Radiat. Meas. 43, 776–780. https://doi.org/10.1016/j.radmeas.2008.01.014.
Murray, A.S., Thomsen, K.J., Masuda, N., Buylaert, J.-P., Jain, M., 2012. Identifying well-bleached quartz using the different bleaching rates of quartz and feldspar luminescence signals. Radiat. Meas. 47, 688–695. https://doi.org/10.1016/j.radmeas.2012.05.006.
Olley, J.M., Pietsch, T., Roberts, R.G., 2004. Optical dating of Holocene sediments from a variety of geomorphic settings using single grains of quartz. Geomorphology 60, 337–358. https://doi.org/10.1016/j.geomorph.2003.09.020.
Pawley, S.M., Toms, P., Armitage, S.J., Rose, J., 2010. Quartz luminescence dating of Anglian Stage (MIS 12) fluvial sediments: comparison of SAR age estimates to the terrace chronology of the Middle Thames valley, UK. Quat. Geochronol. 5, 569–582. https://doi.org/10.1016/j.quageo.2009.09.013.
Peng, J., Li, B., 2017. Single-aliquot regenerative-dose (SAR) and standardised growth curve (SGC) equivalent dose determination in a batch model using the R package 'numOSL'. Anc. TL 35, 32–53.
Peng, J., Li, B., More, J., Garbow, B., Hillstrom, K., Burkhardt, J., Gilbert, P., Varadhan, R., 2018. numOSL: numeric routines for optically stimulated luminescence dating. R package version 2.6. https://CRAN.R-project.org/package=numOSL.
Powell, R., Hergt, J., Woodhead, J., 2002. Improving isochron calculations with robust statistics and the bootstrap. Chem. Geol. 185, 191–204. https://doi.org/10.1016/S0009-2541(01)00403-X.
Prescott, J.R., Hutton, J.T., 1994. Cosmic ray contribution to dose rates for luminescence and ESR dating: large depths and long-term time variations. Radiat. Meas. 23, 497–500. https://doi.org/10.1016/1350-4487(94)90086-8.
Preusser, F., 1999a. Luminescence dating of fluvial sediments and overbank deposits from Gossau, Switzerland: fine grain dating. Quat. Geochronol. 18, 217–222. https://doi.org/10.1016/s0277-3791(98)00054-7.
Preusser, F., 1999b. Lumineszenzdatierung fluviatiler Sedimente: Fallbeispiele aus der Schweiz und Norddeutschland, 3/1999. In: Herbig, H.G. (Ed.), Kölner Forum für

Geologie und Paläontologie. Geologisches Institut der Universität zu Köln, Köln, pp. 1–62, 1999b.
Preusser, F., Müller, B.U., Schüchter, C., 2001. Luminescence dating of sediments from Luthern Valley, Central Switzerland, and implications for the chronology of the last glacial cycle. Quat. Res. (Tokyo) 55, 215–222. https://doi.org/10.1006/qres.2000.2208.
Preusser, F., Reitner, J.M., Schlüchter, C., 2010. Distribution, geometry, age and origin of overdeepened valleys and basins in the Alps and their foreland. Swiss J. Geosci. 103, 407–426. https://doi.org/10.1007/s00015-010-0044-y.
Preusser, F., Ramseyer, K., Schlüchter, C., 2006. Characterisation of low OSL intensity quartz from the NewZealand Alps. Radiat. Meas. 41, 871–877. https://doi.org/10.1016/j.radmeas.2006.04.019.
Preusser, F., Graf, H.R., Keller, O., Krayss, E., Schlüchter, C., 2011. Quaternary glaciation history of northern Switzerland. E&G J. Quat. Sci. 60, 282–305. https://doi.org/10.3285/eg.60.2-3.06.
Preusser, F., Muru, M., Rosentau, A., 2014. Comparing different post-IR IRSL approaches for the dating of Holocene coastal foredunes from Ruhnu Island, Estonia. Geochronometria 41, 342–351. https://doi.org/10.2478/s13386-013-0169-7.
Preusser, F., Büschelberger, M., Kemna, H.A., Miocic, J., Mueller, D., May, J.-H., 2021. Exploring possible links between Quaternary aggradation in the Upper Rhine Graben and the glaciation history of northern Switzerland. Int. J. Earth Sci. 1–20. https://doi.org/10.1007/s00531-021-02043-7.
Reimann, T., Thomsen, K.J., Jain, M., Murray, A.S., Frechen, M., 2012. Single-grain dating of young sediments using the pIRIR signal from feldspar. Quat. Geochronol. 11, 28–41. https://doi:10.1016/j.quageo.2012.04.016.
Rhodes, E.J., 2015. Dating sediments using potassium feldspar single-grain IRSL: initial methodological considerations. Quat. Int. 362, 14–22. https://doi.org/10.1016/j.quaint.2014.12.012.
Salcher, B.C., Starnberger, R., Götz, J., 2015. The last and penultimate glaciation in the North Alpine Foreland: new stratigraphical and chronological data from the Salzach glacier. Quat. Int. 388, 218–231. https://doi.org/10.1016/j.quaint.2015.09.076.
Schielein, P., Schellmann, G., Lomax, J., Preusser, F., Fiebig, M., 2015. Chronostratigraphy of the hochterrassen in the lower lech valley (northern alpine foreland). E&G J. Quat. Sci. 64, 15–28. https://doi.org/10.3285/eg.64.1.02.
Schwenk, M.A., Schläfli, P., Bandou, D., Gribenski, N., Douillet, G.A., Schlunegger, F., 2022. From glacial erosion to basin overfill: a 240 m-thick overdeepening–fill sequence in Bern, Switzerland. Sci. Drill. 30, 17–42. https://doi.org/10.5194/sd-30-17-2022.
Smedley, R.K., 2014. Testing the Use of Single Grains of K-Feldspar for Luminescence Dating of Proglacial Sediments in Patagonia. Aberystwyth University, p. 265. PhD thesis.
Smedley, R.K., Buylaert, J.-P., Újvári, G., 2019. Comparing the accuracy and precision of luminescence ages for partiallybleached sediments using single grains of K-feldspar and quartz. Quat. Geochronol. 53, 101007 https://doi.org/10.1016/j.quageo.2019.101007.
Spencer, J.Q., Owen, L.A., 2004. Optically stimulated luminescence dating of Late Quaternary glaciogenic sediments in the upper Hunza valley: validating the timing of glaciation and assessing dating methods. Quat. Sci. Rev. 23, 175–191. https://doi.org/10.1016/s0277-3791(03)00220-8.
Spooner, N.A., 1994. On the optical dating signal of quartz. Radiat. Meas. 23, 593–600. https://doi.org/10.1016/1350-4487(94)90105-8.
Thiel, C., Buyleart, J.P., Murray, A.S., Terhost, B., Hofer, I., Tsukamoto, S., Frechen, M., 2011a. Luminescence dating of the Stratzing loess profile (Austria) – testing the potential of an elevated temperature post-IR IRSL protocol. Quat. Int. 234, 23–31. https://doi:10.1016/j.quaint.2010.05.018.
Thiel, C., Buyleart, J.P., Murray, A.S., Tsukamoto, S., 2011b. On the applicability of post-IR IRSL dating to Japanese loess. Geochronometria 38, 369–378. https://doi:10.2478/s13386-011-0043-4.
Thrasher, I.M., Mauz, B., Chiverrell, R.C., Lang, A., 2009. Luminescence dating of glaciofluvial deposits: a review. Earth Sci. Rev. 97, 133–146. https://doi:10.1016/j.earscirev.2009.09.001.
Thomsen, K.J., Murray, A.S., Jain, M., Bøtter-Jensen, L., 2008. Laboratory fading rates of various luminescence signals from feldspar-rich sediment extracts. Radiat. Meas. 43, 1474–1486. https://doi:10.1016/j.radmeas.2008.06.002.
Timar, A., Vandenberghe, D.A., Panaiotu, E.C., Panaiotu, C.G., Necula, C., Cosma, C., van den haute, P., 2010. Optical dating of Romanian loess using fine-grained quartz. Quat. Geochronol. 5, 143–148. https://doi.org/10.1016/j.quageo.2009.03.003.
Timar-Gabor, A., Vandenberghe, D.A., Vasiliniuc, S., Panaoitu, E.E., Dimofte, D., Cosma, C., 2011. Optical dating of Romanian loess: a comparison between silt-sized and sand-sized quartz. Quat. Int. 240, 62–70. https://doi.org/10.1016/j.quaint.2010.10.007.
Trauerstein, M., Lowick, S.E., Preusser, F., Rufer, D., Schlunegger, F., 2012. Exploring fading in single grain feldspar IRSL measurements. Quat. Geochronol. 10, 327–333. https://doi:10.1016/j.quageo.2012.02.004.
Trauerstein, M., Lowick, S.E., Preusser, F., Veit, H., 2017. Testing the suitability of dim sedimentary quartz from northern Switzerland for OSL burial dose estimation. Geochronometria 44, 66–76. https://doi.org/10.1515/geochr-2015-0058.
Wintle, A.G., 1973. Anomalous fading of thermoluminescence in mineral samples. Nature 245, 143–144. https://doi.org/10.1038/245143a0.
Wintle, A.G., 2008. Luminescence dating: where it has been and where it is going. Boreas 37, 471–482. https://doi.org/10.1111/j.1502-3885.2008.00059.x.
Wyssling, G., 2008. Geologischer Atlas der Schweiz. 1092 Uster (Atlasblatt 128). Erläuterungen, Bundesamt für Landestopografie, Swisstopo, Wabern.
Zhang, J., Li, S.-H., 2020. Review of the post-IR IRSL dating protocols of K-feldspar. Methods Protoc 3 (7), 1–20. https://doi.org/10.3390/mps3010007.
Ziegler, P.A., Fraefel, M., 2009. Response of drainage systems to Neogene evolution of the Jura fold-thrust belt and upper rhine graben. Swiss J. Geosci. 102, 57–75. https://doi.org/10.1007/s00015-009-1306-4.